Check for updates

Journal of the American Ceramic Society

RESEARCH ARTICLE OPEN ACCESS

Coupled Experimental Study and Thermodynamic Modeling of GeO_2 and GeO_2–CaO and GeO_2–SiO_2 Binary Systems

Saleh Rasouli-Jouryabi | Elmira Moosavi-Khoonsari

Department of Mechanical Engineering, École De Technologie Supérieure (ÉTS), Montréal, Québec, Canada

Correspondence: Elmira Moosavi-Khoonsari (Elmira.moosavi@etsmtl.ca)

Received: 8 August 2025 | **Revised:** 30 December 2025 | **Accepted:** 20 January 2026

Keywords: calcium germanates | CALPHAD | GeO_2–CaO system | GeO_2–SiO_2 system | phase diagram | thermodynamic modeling

ABSTRACT

The phase diagram of the GeO_2–CaO system was investigated using differential thermal–thermogravimetric analysis and the equilibration–quenching technique, followed by electron probe microanalysis and X-ray diffraction. The $Ca_2Ge_7O_{16}$ compound was confirmed to be stable, and a eutectic reaction of L → GeO_2(hex) + $Ca_2Ge_7O_{16}$ was identified in the GeO_2-rich region. Based on the previous and present experimental data for the GeO_2–CaO system and reliable literature data for the GeO_2–SiO_2 system, thermodynamic optimization of both binaries was carried out. The GeO_2–SiO_2 system was reoptimized to ensure internal consistency and improved agreement with experimental data relative to the previous assessment, based on refinements to the heat capacity of GeO_2 and the quartz solid-solution model. The liquid phase was modeled using the Modified Quasichemical Model, and the quartz solid solution in the GeO_2–SiO_2 system, in which Si^{4+} and Ge^{4+} cations are mixed over a single sublattice, was described using the Compound Energy Formalism. A single set of self-consistent Gibbs energy functions for all phases in the GeO_2–CaO and GeO_2–SiO_2 systems was obtained, reproducing phase equilibria and thermodynamic properties over wide composition and temperature ranges. The optimized database provides a reliable foundation for thermodynamic modeling of GeO_2–CaO–SiO_2 ternary and multicomponent oxide systems relevant to metallurgical recycling as well as ceramic-glass design and processing.

1 | Introduction

Germanium, with a total abundance of only 1–1.7 ppm in the Earth's crust, is classified as a critical raw material due to its limited availability and strategic importance [1]. Of the approximately 12,558 t/year of extractable Ge in primary resources, less than 1% (~118 t/year) is converted into products, with the remainder lost as waste [2]. This exceptionally high dissipation rate, coupled with the growing demand for Ge in electronics and telecommunications (e.g., infrared detectors, solar panels, and optical fibers), heightens serious concerns regarding supply security [1–4]. Because germanium rarely occurs in concentrated minerals, it is mainly obtained as a byproduct of zinc, lead, and copper extraction and from coal combustion residues [4]. Enhancing recycling rates (currently well below the 50% target) and reducing processing losses are essential for improving overall supply-chain efficiency [5]. Industrial residues such as slags [6, 7], dusts [7], and leaching residues [8, 9], as well as end-of-life products [7, 10], represent promising secondary sources for Ge recovery.

Despite its technological and strategic importance, the thermodynamic behavior of GeO_2 and its interactions with other oxides remain poorly understood. Reliable phase equilibria and thermodynamic data are limited, and in some cases inconsistent, which complicates process modeling and recycling strategies. Among binary systems involving GeO_2, the GeO_2–CaO and GeO_2–SiO_2 systems are of particular industrial relevance because CaO and SiO_2 are the dominant constituents of metallurgical slags, coal ash, and glassy residues encountered in recycling

This is an open access article under the terms of the Creative Commons Attribution License, which permits use, distribution and reproduction in any medium, provided the original work is properly cited.

© 2026 The Author(s). *Journal of the American Ceramic Society* published by Wiley Periodicals LLC on behalf of The American Ceramic Society.

and refining operations [6–9]. The GeO_2–CaO binary system is applied in optical and luminescent materials, including glass-ceramics and radiation-shielding glasses [11–15]. The GeO_2–SiO_2 binary system is widely used in optical fibers, photonic devices, high-performance glasses, and low-thermal-expansion materials [12, 16, 17].

The present study develops a self-consistent thermodynamic description of the GeO_2–CaO and GeO_2–SiO_2 binary systems using the CALPHAD (CALculation of PHAse Diagrams) approach. In CALPHAD optimization, all available thermodynamic and phase equilibrium data are critically evaluated and simultaneously fitted to obtain Gibbs energy functions for all relevant phases as functions of temperature and composition. Thermodynamic property data, such as activity, can aid in the evaluation of the phase diagram, and phase diagram measurements can be used to deduce thermodynamic properties. From the Gibbs energy equations, all the thermodynamic properties and phase diagrams can be back-calculated. This methodology ensures internal consistency and consistency with thermodynamic principles among thermodynamic properties and phase equilibria, allowing for reliable interpolation and extrapolation within the assessed systems.

In this work, the phase diagram measurements of Shirvinskaya et al. [18] and Grebenshchikov et al. [19] were re-examined, and new experiments were conducted under well-defined conditions using differential thermal analysis (DTA), thermogravimetric analysis (TGA), and the equilibration–quenching–phase identification technique. The DTA-TGA method was used to detect phase transitions, while equilibration–quenching–phase identification complemented these measurements by confirming and quantifying the equilibrium phases and phase boundaries. The newly obtained phase equilibrium data resolved discrepancies in the literature and were used to refine model parameters. The resulting optimized database enables reliable prediction of phase stabilities, thermodynamic properties, and activities over a wide range of temperatures and compositions.

The present work forms part of a broader effort to establish a comprehensive thermodynamic database for GeO_2-containing systems. The database, compatible with FactSage, provides a robust foundation for modeling and optimizing Ge extraction and recycling processes, as well as for designing Ge-based ceramic and glass materials.

2 | Availability of Data on the Systems' Constituents

In the current study, the thermodynamic descriptions of pure components were adopted from FactSage 8.2 and its databases, where available and considered reliable. The $\Delta H^o_{298\ K}$ and $S^o_{298\ K}$ of GeO_2(s,l), CaO(s), and SiO_2(s,l) as well as C_p of CaO(s,l) and SiO_2(s,l), were adopted from the FactSage 8.2 FToxid database. The C_p of GeO_2(s,l) were re-evaluated and reoptimized in this work. The melting temperature of CaO was also re-evaluated and reoptimized, based on which the $\Delta H^o_{298\ K}$ and $S^o_{298\ K}$ of CaO(l) were newly calculated. Gas phase thermodynamic properties were taken from the FactSage 8.2 FactPS database, originally based on the Barin and Platzki [20] compilation. All available data for the GeO_2–CaO and GeO_2–SiO_2 binary systems were also collected, encompassing both stoichiometric compounds and solid and liquid solutions.

2.1 | Pure Components

2.1.1 | GeO_2

Germanium oxide exists in two solid polymorphs: a low-temperature tetragonal phase with rutile-type symmetry and a high-temperature hexagonal phase with β-quartz-type symmetry [12]. The polymorphic transition between these forms has been reported to occur between 1281 K [21] and 1310 K [22] and is known to be extremely sluggish, allowing the high-temperature hexagonal phase to persist metastably at room temperature [21]. Furthermore, similar to SiO_2, GeO_2 forms a highly viscous glassy phase upon melting, causing the amorphous phase to remain stable at lower temperatures [23].

Owing to its distinct electrical properties, GeO_2 has attracted considerable interest, resulting in several experimental studies aimed at determining its thermodynamic properties. In this work, these experimental measurements were compared with the FactSage 8.2 FToxid database. Some differences identified between reliable literature data and the existing FactSage optimization prompted a re-evaluation and reoptimization of the C_p equations for GeO_2. A similar reoptimization of the C_p of GeO_2 has been previously reported [12, 24], in agreement with the present optimization. The values of $\Delta H^o_{298\ K}$ and $S^o_{298\ K}$ obtained from FactSage were found to be consistent with experimentally reported data [22, 25] and those documented in the Barin and Platzki [20] compilation, and were, therefore, adopted in this work.

For low-temperature tetragonal GeO_2, C_p data were obtained using low-temperature adiabatic calorimetry by Counsell and Martin [26] and high-temperature drop calorimetry by Andon and Mills [27]. Both studies used the same high-purity sample (99.9976%), providing a consistent dataset and minimizing associated errors. These results were subsequently incorporated into standard reference works by Barin and Platzki [20] and Gurvich et al. [25]. Based on these sources, a revised temperature-dependent polynomial expression for the C_p of tetragonal GeO_2 in the range 298.15–1308 K was developed in this study.

For high-temperature hexagonal GeO_2, King [28] reported low-temperature drop calorimetry data using a copper vessel. Kelley and Christensen [29] further measured the heat content (H_T–$H_{298\cdot15K}$) using drop calorimetry with a copper vessel, while preventing GeO_2 sublimation by sealing the powder in a Pt-Rh tube. These measurements were subsequently included in reference works by Barin and Platz [20] and Gurvich et al. [25]. Additionally, Richet [23] provided relatively consistent experimental data for the hexagonal polymorph in the range 760–1372 K using an ice calorimeter on samples with 99.999% purity. These datasets were combined to derive a new temperature-dependent polynomial expression for the C_p of hexagonal GeO_2 in the range 298.15–1388 K.

For the glassy and liquid phases of GeO_2, low-temperature C_p data from drop calorimetry by Tarasov and Soboleva [30] were

15512916, 2026, 2, Downloaded from https://ceramics.onlinelibrary.wiley.com/doi/10.1111/jace.70551 by Ecole De Technologie Superieur, Wiley Online Library on [25/03/2026]. See the Terms and Conditions (https://onlinelibrary.wiley.com/terms-and-conditions) on Wiley Online Library for rules of use; OA articles are governed by the applicable Creative Commons License

combined with high-temperature heat content measurements by Kelley and Christensen [29]. Using a similar polynomial fitting approach, a continuous C_p expression was derived, valid over the temperature range 298.15–2000 K. The optimized C_p values are presented in Section 6.

Furthermore, several studies have measured the vapor pressure above pure GeO_2, using Knudsun effusion mass spectrometry (KEMS) [31–34]. These investigations indicate that the predominant gas species above pure GeO_2 at elevated temperatures is GeO(g), corresponding to the following sublimation reaction:

$$GeO_2(s) = GeO(g) + 1/2O_2(g) \quad (1)$$

Davydov and Neorg [31] and Shimazaki et al. [33] conducted their experiments using quartz crucibles; however, due to the significant solid-state solubility between SiO_2 and GeO_2, their results likely include operational errors. Another key requirement of KEMS measurements is achieving equilibrium by establishing a saturated vapor pressure over the condensed phase (either solid or liquid). Sasamoto et al. [29] did not meet this equilibrium condition, leading to an underestimation of vapor pressure values, as noted by Smirnov et al. [34]. In their more recent study, Smirnov et al. [34] addressed these issues by using an Alundum cell to prevent contamination and implementing improved heating cycles to ensure equilibrium was achieved within the temperature range of 1250–1370 K.

Moreover, the theoretical fitting model developed by Knudsun in 1909 [35] requires ideal effusion during experiments (i.e., ideal molecular flow), which may not always be achieved in practice. Motzfeldt's correction improves the accuracy of thermodynamic data derived from KEMS by accounting for nonideal conditions, such as molecular interactions between gas species (primarily GeO and O_2 in this system) and cell geometry [34]. Rather than considering only the partial pressure of GeO(g), it is more appropriate to also include other gaseous species involved in the reaction, namely, O_2(g). Therefore, the equilibrium constant of reaction (1) was calculated using P_{GeO} and P_{O_2}, corrected using Motzfeldt's empirical equation. Among the available studies, Smirnov et al. [34] applied both ideal and nonideal effusion models and concluded that the nonideal treatment, particularly with Motzfeldt's correction, provided better agreement with experimental observations. In contrast, the other three studies [31–33] fitted their ion current data using the ideal effusion model and did not report P_{O_2} from their KEMS measurements. Smirnov et al. [34] provided three datasets of P_{GeO} and P_{O_2}, which were used in this work to calculate the equilibrium constant ($K_1 = P_{GeO} \cdot P_{O_2}^{1/2}$) for the sublimation reaction, that is, Equation (1). A comparison between these experimental measurements and the calculations from this study is presented in Section 6.1.

2.1.2 | SiO_2 and CaO

In this study, the FToxid database in FactSage 8.2 was used as the source of thermodynamic data for SiO_2 and CaO. However, the melting temperature of CaO was revised based on more recent investigations reporting higher values [36, 37]. This update addresses a controversy, first raised by Foex [38] and later by Yamada et al. [39] in 1965 and 1986, respectively, who for the first time applied a self-crucible approach, thereby eliminating possible reactions between the sample and its container.

Accurately measuring the melting point of CaO, an extremely refractory material, is highly challenging, as it typically requires optical pyrometry at temperatures above 2500 K [37]. CaO exhibits unique high-temperature optical properties, historically referred to as "limelight," which complicate the determination of its emissivity during pyrometric measurements [36, 37]. The state of CaO can also be affected by contamination from surrounding materials and by the experimental atmosphere. This may lead to oxygen deficiency, formation of substoichiometric CaO_{1-x}, and incongruent melting, thereby underestimating the true congruent melting point of stoichiometric CaO, particularly under reducing conditions. Consequently, experiments under oxidizing atmospheres, which stabilize stoichiometric CaO, are recommended to accurately determine its congruent melting point [36].

Furthermore, the strong tendency of CaO to readily react with atmospheric H_2O and CO_2, and the subsequent release of these species during heating, can complicate both the experimental procedures and the resulting data when compared with other refractory oxides. This inherent reactivity must also be considered when evaluating the large discrepancies observed in reported melting point data [36].

To address these challenges, Manara et al. [37] prepared CaO samples from high-purity (99.998%) CaO powder, pressed into pellets, and presintered in argon to remove hydroxide and carbonate impurities. Melting experiments were conducted in a controlled-atmosphere laser-heating cell equipped with a gas-proof quartz window. The samples were held by graphite screws in a self-crucible, containerless setup, and heated using a 4.5 kW Nd:YAG laser focused on the sample surface. It was reported that the rapid heating and short melt duration minimized vaporization and contamination, while fast pyrometry allowed accurate measurement of melting and freezing temperatures under different gas atmospheres (up to 0.3 MPa) [37]. Similarly, Bgasheva et al. [36] pressed high-purity CaO powders (99.8–99.998%) into pellets followed by heat-treatment in argon at 1670 K to remove residual hydroxide and carbonate phases. Melting tests were performed using combined laser heating; that is, a CO_2 laser for gradual temperature increase and an Nd:YAG laser for precise, homogeneous heating. It was reported that this method ensured excellent temperature control and minimized contamination, offering greater flexibility than image or solar furnaces. The use of laser heating avoided supercooling artifacts and enabled accurate identification of melting and solidification temperatures [36]. Therefore, an accurate measurement of the CaO melting point requires a controlled atmosphere, high-quality pyrometry equipment, and suitable sample containers to prevent contamination.

Experimental measurements [36–44] and modeling studies [45–48] have reported melting points for CaO across a wide range, from 2838 to 3222 K (see Table 1). These values can be grouped into two distinct clusters: one centered around 2860 K ± 48 K and another around 3170 K ± 23 K. The discrepancy between these recent measurements and the 2845 K value used in FactSage 8.2 is understandable, as the optimization by Eriksson and Pelton [49] dated back to 1993, when most available experimental

15512916, 2026, 2, Downloaded from https://ceramics.onlinelibrary.wiley.com/doi/10.1111/jace.70551 by Ecole De Technologie Superieur, Wiley Online Library on [25/03/2026]. See the Terms and Conditions (https://onlinelibrary.wiley.com/terms-and-conditions) on Wiley Online Library for rules of use; OA articles are governed by the applicable Creative Commons License

TABLE 1 | Melting points and enthalpies of fusion for CaO from experimental and computational studies, with associated conditions.

Melting point (K)	ΔH_f^o (kJ/mol)	Technique		Atmosphere	Crucible	Ref.
		Experiment	Modeling			
2887	—	Graphite furnace	—	H_2	W	[41]
2838	—	Conventional heating	—	—	W	[44]
2898	—	Induction furnace	—	N_2	Self-crucible	[40]
3183	—	Solar furnace	—	Air	Self-crucible	[38]
2858	—	Solar furnace	—	Air	Self-crucible	[42]
2890	—	Induction furnace	—	$CO + CO_2 + N_2$	Self-crucible	[43]
3172	—	Arc imaging furnace	—	Air	No crucible	[39]
3210	74.5	—	MD[b]	—	—	[47]
3222	—	Nd-YAG[a] laser heating	—	Air	Self-crucible	[37]
3192	—		—	$Ar + 6\%H_2$		
3156	80.89	—	MD + AIMD[c]	—	—	[45]
3164	—	Nd-YAG and CO_2 laser heating	—	Ambient	Self-crucible	[36]
3157	—		—			
2767	—	—	MD	—	—	[48]
3066	80.37	—	Void nucleated MD	—	—	[46]
2940	—	—	Two-phase coexistence	—	—	
3200	79.5	—	NIST-JANAF	—	—	[50]
2845	79.496	—	FactSage 8.2 FToxid	—	—	[49]

[a]Yttrium aluminum garnet.
[b]Molecular dynamics.
[c]Ab initio molecular dynamics.

data fell within the lower temperature range. In this study, the melting point of CaO was re-evaluated based on the most recent experimental and modeling results. The adopted value, 3200 K, is taken from the NIST–JANAF Thermochemical Tables [50], aligning more closely with recent high-temperature data.

2.2 | Binary Systems

2.2.1 | GeO_2–CaO Binary

Several stoichiometric compounds have been reported in the GeO_2–CaO binary system. Tricalcium germanate ($3CaO{\cdot}GeO_2 = Ca_3GeO_5$) was synthesized at 1773 K by Royak and Prokhvatilova [51]. Ca_3GeO_5 was reported to be stable only above 1593 K; below this temperature, it decomposes into CaO and Ca_2GeO_4 [51, 52]. Shirvinskaya et al. [18] and Grebenshchikov et al. [19] reported that the compound melts incongruently at approximately 2153 K. It exists in several metastable polymorphic forms [51, 52], appearing in both monoclinic and triclinic structures at room temperature, which are considered deformations of a rhombohedral high-temperature modification. The monoclinic phase is the more stable form, transforming into the triclinic structure after short-term annealing [52].

Dicalcium germanate ($2CaO{\cdot}GeO_2 = Ca_2GeO_4$) has been synthesized via solid-state sintering at 1373–1673 K, exhibiting thermal stability and structural similarity to its silicate analogue [51–55]. Shirvinskaya et al. [18] and Grebenshchikov et al. [19] reported that the compound melts congruently at approximately 2173 K. Eulenberger et al. [56] confirmed that Ca_2GeO_4 adopts an olivine-type structure, consistent with pattern lines previously observed by Royak and Prokhvatilova [51]. According to Toropov and Shirvinskaya [57], Ca_2GeO_4 crystallizes in two polymorphic forms: a low-temperature phase with an olivine-type structure, and a high-temperature phase, stable above 1723 K, that is structurally identical to α-Ca_2SiO_4 based on X-ray diffraction (XRD) data.

Tricalcium digermanate ($3CaO{\cdot}2GeO_2 = Ca_3Ge_2O_7$) was reported by Shirvinskaya et al. [18] and Grebenshchikov et al. [19] as an incongruently melting compound, decomposing into Ca_2GeO_4 and liquid at 1683 K. Its formation was confirmed by XRD and infrared spectroscopy, and it was described as analogous to $Ca_3Si_2O_7$ (rankinite). Marychev et al. [58] also reported the existence of another stoichiometric compound, $Ca_5Ge_3O_{11}$, at 62.5 mol% CaO, a composition very close to $Ca_3Ge_2O_7$. They synthesized $Ca_5Ge_3O_{11}$ using a flux method for single-crystal growth. However, it should be noted that compounds obtained through solution-based synthesis are not always reproducible under the high-temperature conditions typically employed in phase equilibrium studies [37, 40].

Eulenberger et al. [56] reported that calcium metagermanate ($CaO{\cdot}GeO_2 = CaGeO_3$) was identified by single-crystal analysis as having a triclinic β-wollastonite-type ($CaSiO_3$) structure, forming

15512916, 2026, 2, Downloaded from https://ceramics.onlinelibrary.wiley.com/doi/10.1111/jace.70551 by Ecole De Technologie Superieur, Wiley Online Library on [25/03/2026]. See the Terms and Conditions (https://onlinelibrary.wiley.com/terms-and-conditions) on Wiley Online Library for rules of use; OA articles are governed by the applicable Creative Commons License

thin, flake-like crystals. Unlike its silicate analogue, $CaGeO_3$ is stable in only one structural form under standard conditions, as noted by Shirvinskaya et al. [18] and Grebenshchikov et al. [19], and it melts congruently at 1693 K.

Eulenberger et al. [56] reported the existence of calcium digermanate ($CaO{\cdot}2GeO_2 = CaGe_2O_5$), in contrast to the previously proposed stoichiometry $Ca_2Ge_3O_8$ by Koelmans and Verhagen [59]. In their study, Eulenberger et al. [56] identified both $CaGeO_3$ and $CaGe_2O_5$ in sintered mixtures with a CaO/GeO_2 molar ratio of 1:1.5, and exclusively $CaGe_2O_5$ at a 1:2 ratio. The identification of $CaGe_2O_5$ is further supported by its structural similarity to titanite ($CaTiSiO_5$) and tilasite ($CaMgAsO_4F$), as well as the identical powder diffraction patterns reported for $Ca_2Ge_3O_8$ and the synthesized $CaGe_2O_5$. Additionally, Shirvinskaya et al. [18] and Grebenshchikov et al. [19] reported that $CaGe_2O_5$ melts congruently at 1558 K.

Eulenberger et al. [56] reported that $CaGe_4O_9$ exists in two polymorphic forms: γ-$CaGe_4O_9$ (low-temperature phase) and β-$CaGe_4O_9$ (high-temperature phase). Shirvinskaya et al. [18] and Grebenshchikov et al. [19] reported that this compound melts congruently at 1593 K. Catauro et al. [60] also reported its formation via thermal synthesis followed by XRD. However, the more recent work by Redhammer et al. [61] revised the stoichiometry to $Ca_2Ge_7O_{16}$, synthesizing the compound through both hydrothermal and powder sintering methods. To compensate for GeO_2 evaporation during sintering, an excess of GeO_2 was added, which appeared as residual peaks in the XRD pattern; thus, the diffraction data from the hydrothermal product were used for structural analysis. Crystallographic characterization confirmed the revised stoichiometry of $Ca_2Ge_7O_{16}$. The earlier misidentification by Catauro et al. [60] likely resulted from the limited crystallographic database resources available at that time.

Shirvinskaya et al. [18] and Grebenshchikov et al. [19], from the same research group, reported the phase diagram of the GeO_2–CaO system in the late 1960s, using DTA, microscopy, crystallo-optical method, and XRD over the temperature range of 298–1673 K. Phase compositions were confirmed using immersion oils, with phosphoric liquids of high refractive indices employed to determine optical properties, while densities were measured by the pycnometric method. Analytical-grade $CaCO_3$ and GeO_2 powders served as starting materials, which were sintered at high temperatures; homogeneity of the germanates was verified for some compositions through repeated annealing and intermediate pulverization. They determined the liquidus and solidus temperatures, identified stable stoichiometric compounds, and established their melting points and melting behavior using DTA. Their work reported four eutectic reactions and suggested the possible formation of a miscibility gap in the narrow range of 86–96 mol% GeO_2, with a critical point near 1643 K, as well as a monotectic reaction at approximately 1553 K. Their interpretations were influenced by the silicate analogue and the GeO_2–MgO phase diagram reported by Robbins and Levin [62], who used the equilibration–quenching method combined with binocular and petrographic microscopy and XRD. Robbins and Levin [62] observed a two-liquid immiscibility region between 66 and 92 mol% GeO_2 in the GeO_2–MgO system, comparable to the two-liquid immiscibility range of 72–99 mol% SiO_2 observed in its silicate analogue (SiO_2–MgO).

Shirvinskaya et al. [18] and Grebenshchikov et al. [19] provided an important first assessment of the general topology of the GeO_2–CaO binary system. However, several experimental details and some equilibrium phase assemblages remain insufficiently documented, leaving room for clarification and refinement. For instance, it was not specified whether TGA was conducted alongside DTA to monitor potential mass loss, a critical consideration in systems containing GeO_2, which exhibits high vapor pressures. The use of open crucibles raises further concerns about mass loss and deviations from nominal compositions, yet no information was provided on measures taken to mitigate these effects. Additionally, the heating and cooling rates used in the DTA experiments were not reported, and thermal/cooling curves were presented only for stoichiometric compounds. As is well known, phase transformation temperatures can shift to higher values due to kinetic effects under nonequilibrium conditions. No mention was made of temperature calibration or correction runs, and the crucible or sample container materials were not identified, leaving the possibility of contamination unaddressed. Similarly, the heating rate for XRD measurements was not specified. The method used to ensure the complete decomposition of $CaCO_3$ was not described, and the polymorphic transition of GeO_2 was not presented in the reported phase diagram. Furthermore, there are also inconsistencies regarding the stability of $CaGe_4O_9$, with some earlier studies reporting it as a stable phase, while more recent investigations suggest the correct stoichiometry corresponds to $Ca_2Ge_7O_{16}$ [18, 19, 60, 61]. In light of these uncertainties and inconsistencies, selective key phase diagram measurements were carried out in the present study to clarify phase relationships, as discussed in Sections 5.1 and 5.2.

Moreover, Shushunov et al. [63] measured the C_p of Ca_2GeO_4 over the temperature range 6–350 K using adiabatic drop calorimetry. The low-temperature C_p data (6–298 K) were used in the present work to derive the $S^o_{298\ K}$, yielding 132.055 J/mol·K. The C_p values from 298 to 350 K were then combined with estimated data at higher temperatures to model the high-temperature C_p behavior, accounting for the compound's very high melting point of approximately 2173 K. This approach is consistent with the C_p behavior of Ca_2SiO_4 reported by Coughlin and O'Brien [64].

2.2.2 | GeO_2–SiO_2 Binary

No stoichiometric compounds have been reported in the GeO_2–SiO_2 system. Instead, hexagonal GeO_2 and hexagonal SiO_2 exhibit substantial mutual solubility in the α-quartz structure at subsolidus temperatures due to their similar crystal structures [7]. Baret et al. [65] conducted experiments across various compositions to determine solidus and liquidus temperatures using equilibration–quenching (10–48 h, depending on temperature) followed by XRD. Based on their measurements, they proposed the following expressions for the excess Gibbs energy: for the solid solution, $\Delta G_S^{ex} = (-17\,700 - 5 \cdot T)\ \cdot X(1-X)$, and for the liquid solution, $\Delta G_L^{ex} = -25\,500 \cdot X(1-X)$, in J/mol, where X is the mole fraction of $Ge_{1/2}O$. Swamy et al. [66] later treated the liquid phase as an ideal solution and suggested a regular solution parameter of 3694 J/mol for the solid solution.

Huffman et al. [67] used solution calorimetry at 973 K to measure the heat of mixing of the liquid solution and reported a

15512916, 2026, 2, Downloaded from https://ceramics.onlinelibrary.wiley.com/doi/10.1111/jace.70551 by Ecole De Technologie Superieur, Wiley Online Library on [25/03/2026]. See the Terms and Conditions (https://onlinelibrary.wiley.com/terms-and-conditions) on Wiley Online Library for rules of use; OA articles are governed by the applicable Creative Commons License

negative deviation from ideality. This result was later questioned by Maniar et al. [68], who attributed the deviation to a small fraction of crystalline cristobalite in Huffman's sample. Maniar et al. [68] conducted transposed-temperature drop calorimetry on flame-hydrolyzed preforms to measure the solution heat content ($H_{973\ K} - H_{298.15\ K}$) and solution calorimetry on preform and annealed glasses in molten lead borate to determine the heats of solution at 973 K. Their results supported ideal mixing behavior for the GeO_2–SiO_2 liquid solution. Accordingly, and considering the similar network-forming behavior of SiO_2 and GeO_2 [69], the ideal mixing assumption for the liquid solution was adopted in this study. The excess Gibbs energy of the quartz solid solution was subsequently adjusted to reproduce the experimental liquidus and solidus data of the phase diagram. The calculated heat content and heat of mixing of the GeO_2–SiO_2 liquid solution at 973 K are compared with the experimental values of Huffman et al. [67] and Maniar et al. [68] in Section 6.2.

3 | Phases and Thermodynamic Models

To establish the stability ranges of the various phases in the phase diagram, the Gibbs energy functions of individual phases were modeled, and phase equilibria were subsequently computed using the Gibbs energy minimizer in FactSage [70]. This section summarizes the thermodynamic models applied to each phase in the studied systems.

3.1 | Stoichiometric Compounds

The Gibbs energy of a stoichiometric compound at 1 atm is expressed by:

$$G_T^o = H_T^o - TS_T^o, \tag{2}$$

$$H_T^o = \Delta H_{298.15\ K}^o + \int_{298.15\ K}^{T} C_P\, dT, \tag{3}$$

$$S_T^o = S_{298.15\ K}^o + \int_{298.15\ K}^{T} \frac{C_P}{T} dT, \tag{4}$$

where G_T^o, H_T^o, and S_T^o are the standard Gibbs energy, enthalpy, and entropy, respectively, of a given compound at absolute temperature T; $\Delta H_{298.15\ K}^o$ is the standard enthalpy of formation of the stoichiometric compound from pure elements at 298.15 K (with $\Delta H_{298.15\ K}^o$ of elemental species stable at 298.15 K and 1 atm assumed to be 0 J/mol as reference); $S_{298.15\ K}^o$ is the standard entropy at 298.15 K; and C_p is the temperature-dependent heat capacity.

The Gibbs energy of solid GeO_2 was reoptimized in this work using the modified C_p data. The Gibbs energies of solid CaO and SiO_2 were adopted from FactSage 8.2 FToxid database, while those of all gaseous species (GeO(g) and O_2(g)) were taken from FactSage 8.2 FactPS database.

3.2 | Liquid Oxide Solution

In this study, the liquid oxide solution was modeled using the Modified Quasichemical Model (MQM), which accounts for short-range ordering (SRO) in molten oxide systems by incorporating second-nearest-neighbor (SNN) cation–cation pair exchange reactions, with oxygen acting as the common anion. The liquid phase in this system consists of CaO, SiO_2, and GeO_2.

In the binary oxide melt, the quasi-chemical reaction can be written as follows [71]:

$$(A-A) + (B-B) = 2(A-B);\ \Delta g_{AB}, \tag{5}$$

where A and B represent the cationic species in the liquid solution, and (A–B) denotes a SNN pair bridged by an oxygen anion. The formation of such SNN pairs introduces SRO, resulting in deviations from ideal mixing. These deviations are captured in the excess Gibbs energy term of the solution. The total Gibbs energy of the liquid solution, including both ideal and excess contributions, is expressed as:

$$G = \left(n_A \cdot g_A^o + n_B \cdot g_B^o\right) - T \cdot \Delta S^{config} + \left(\frac{n_{AB}}{2}\right) \cdot \Delta g_{AB}, \tag{6}$$

where n_i and g_i^o are the number of moles and molar Gibbs energies of the pure components, respectively; n_{AB} is the number of moles of (A − B) pairs at equilibrium; Δg_{AB} is the Gibbs energy of formation of the (A − B) pairs; and ΔS^{config} is the configurational entropy associated with the random distribution of (A − A), (B − B), and (A − B) pairs under the ideal mixing approximation:

$$\Delta S^{conf.} = -R\left(n_A \cdot lnX_A + n_B \cdot lnX_B\right) - R\left[n_{AA} \cdot ln\ \left(X_{AA}/Y_A^2\right) + n_{BB} \cdot ln\ \left(X_{BB}/Y_B^2\right) + n_{AB} \cdot ln\left(X_{AB}/2Y_AY_B\right)\right], \tag{7}$$

where n_{ij} is the number of moles of (i − j) pairs, X_i is the mole fraction, X_{ij} is the pair fraction, and Y_i is the coordination-equivalent fraction, defined as follows to account for composition-dependent coordination numbers:

$$Y_A = \frac{Z_An_A}{Z_An_A + Z_Bn_B} = \frac{Z_AX_A}{Z_AX_A + Z_BX_B} = 1 - Y_B, \tag{8}$$

where Z_i is the coordination number of i.

Δg_{AB} is described as a function of pair fractions:

$$\Delta\, g_{AB} = \Delta g_{AB}^o + \sum_{i\geq 1} g_{AB}^{i0} \cdot X_{AA}^i + \sum_{j\geq 1} g_{AB}^{0j} \cdot X_{BB}^j, \tag{9}$$

where Δg_{AB}^o, g_{AB}^{i0}, and g_{AB}^{0j} are model parameters for the liquid solution, which may be temperature-dependent. Detailed descriptions of the MQM as applied to binary systems are available in the literature [71].

In this work, the cationic species (A or B in Equation 5) are Ca^{2+}, Si^{4+}, and Ge^{4+}. The Gibbs energy of liquid SiO_2 was adopted from the FactSage 8.2 FToxid database, while the Gibbs energies of pure liquid CaO and GeO_2 were optimized as part of this study. To ensure consistency between the newly developed database and

15512916, 2026, 2, Downloaded from https://ceramics.onlinelibrary.wiley.com/doi/10.1111/jace.70551 by Ecole De Technologie Superieur, Wiley Online Library on [25/03/2026]. See the Terms and Conditions (https://onlinelibrary.wiley.com/terms-and-conditions) on Wiley Online Library for rules of use; OA articles are governed by the applicable Creative Commons License

existing assessments, thereby facilitating broader applicability, the coordination numbers for Ca^{2+} and Si^{4+} were adopted from previous evaluations (e.g., the $CaO–SiO_2$ system developed by Jung et al. [72]). The coordination number for Ge^{4+} was fixed at 2.7548, analogous to that used for Si^{4+}.

3.3 | Quartz Solid Solution

A quartz-type solid solution forms in the $GeO_2–SiO_2$ system, where Si and Ge cations are each coordinated by four O anions, forming corner-sharing tetrahedra [73]. This solution can be structurally represented as $[Si^{4+}, Ge^{4+}]^C(O_2)^A$, where the cations are mixed over a single sublattice. The end-members correspond to pure GeO_2 and pure SiO_2, with no vacancies considered in either the cation or anion sublattice, as crystallographic studies have not indicated any significant vacancy concentrations [73]. This solid solution was thermodynamically modeled using the Compound Energy Formalism (CEF) [74]. The general expression for the solution is given as:

$$G^m = \sum_i y_i^C G_i - TS_C + G^E, \tag{10}$$

where y_i^C denotes the site fraction of constituent i on the C sublattice; G_i is the Gibbs energy of the end-member $(i)^C O_2$, where the C sites are occupied by cation i; S_C is the configurational entropy, assuming random mixing on the C sublattice,

$$S_C = -R\left(\sum_i y_i^C ln y_i^C\right) \tag{11}$$

and G^E is the excess Gibbs energy, which can be expanded in the Redlich–Kister form,

$$G^E = y^C_{Ge^{4+}} y^C_{Si^{4+}} \sum_{i\geq 0} L^i_{Ge^{4+},Si^{4+}} \left(y^C_{Ge^{4+}} - y^C_{Si^{4+}}\right)^i, \tag{12}$$

where L^i represents the interaction energy between Ge^{4+} and Si^{4+} cations on the C sublattice. This parameter quantifies the deviation from ideal mixing and can be adjusted during model optimization as needed.

4 | Experimental and Analytical Methods

The phase diagram for the binary system $GeO_2–CaO$ was calculated following a critical evaluation of available literature data and preliminary optimization of model parameters. This process identified key regions within the phase diagrams, which guided the design of targeted experiments to generate new data and enhance the accuracy of the thermodynamic models. The experimental methods employed included: (1) dynamic measurements using DTA coupled with TGA, and (2) static measurements based on the equilibration and quenching technique, followed by microstructural characterization through scanning electron microscopy with energy-dispersive spectroscopy (SEM-EDS), electron probe microanalysis (EPMA), and XRD.

In this study, DTA-TGA and the equilibrium–quenching technique were employed in a complementary manner to obtain a better understanding of the $GeO_2–CaO$ system. DTA-TGA was used to identify phase transitions and thermal events, providing insight into transformation temperatures and reaction sequences; however, its interpretation can be influenced by the heating rate, kinetic limitations, and GeO_2 volatility, which can obscure thermal signals and complicate quantitative analysis. Slow heating facilitates reproducible phase transitions, but excessively slow rates or prolonged runs may cause pressure buildup and capsule rupture. To overcome such limitations, controlled intermediate annealing and multiple heating–cooling cycles were applied. Quantitative phase determination and definition of phase boundaries were achieved through equilibration–quenching combined with XRD and EPMA, allowing direct observation and analysis of equilibrium phases. Although GeO_2 volatilization remains a challenge, careful design of equilibration time can minimize its effects. The addition of CaO may enhance reaction kinetics and reduce viscosity, as tentatively interpreted from kinetic studies reporting similar effects of alkali oxides such as Li_2O and K_2O [21]. Interpretations of phase transitions and phase equilibria were based on both the experiments and thermodynamic principles. Overall, the combination of both techniques provides a robust and complementary framework: DTA-TGA for detecting transition temperatures and equilibration–quenching–XRD–EPMA for confirming and quantifying equilibrium phases and their compositions.

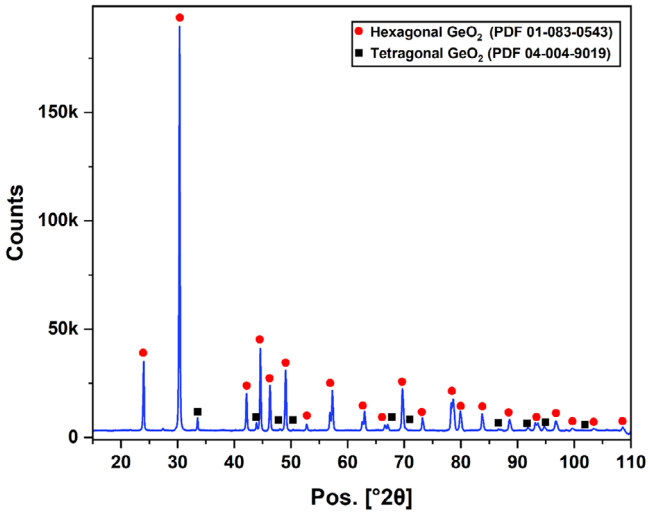

FIGURE 1 | XRD pattern of pure GeO_2, as-received.

4.1 | Starting Materials and Sample Preparation

Ultra-pure germanium oxide (GeO_2, 99.9999%) and calcium oxide (CaO, 99.95%) powders from Alfa Aesar (Massachusetts, USA) were used to prepare the mixtures. Prior to the main experiments, XRD analysis was performed to verify the purity of each powder. The results showed that the GeO_2 powder predominantly consisted of the hexagonal polymorph, the stable high-temperature phase. This is likely due to the atomization production method, which involves extremely rapid cooling that effectively quenches each particle, stabilizing the high-temperature structure at room temperature. Figure 1 presents the XRD pattern of the as-received GeO_2 powder.

15512916, 2026, 2, Downloaded from https://ceramics.onlinelibrary.wiley.com/doi/10.1111/jace.70551 by Ecole De Technologie Superieur, Wiley Online Library on [25/03/2026]. See the Terms and Conditions (https://onlinelibrary.wiley.com/terms-and-conditions) on Wiley Online Library for rules of use; OA articles are governed by the applicable Creative Commons License

The presence of significant hydroxides in the CaO powder, as revealed by XRD, required water removal before the main experiments. Following literature recommendation [75], the CaO powder was heated at 1273 K for 4 h in a platinum crucible inside a box furnace to eliminate hydroxide impurities. After heating, the powder was cooled to room temperature under vacuum in a desiccator and then stored in an oven to prevent moisture reabsorption. The GeO_2 powder was also stored in the oven before use. Just prior to the experiments, both powders were cooled to room temperature in a vacuum desiccator to minimize moisture uptake.

For mixture preparation, appropriate amounts of powders were manually blended using a sapphire mortar with low-water-content isopropanol (H_2O content < 0.05 wt%) as the mixing medium. The resulting mixtures were quickly dried under a heating lamp and stored in the oven. Due to the high vapor pressure of GeO_2, samples were sealed in high-purity platinum capsules (99.95%) measuring 7 mm in length, 4 mm outer diameter, and 3 mm inner diameter, using a micro TIG welder to minimize mass loss during measurements.

4.2 | Thermal Analysis

Dynamic phase diagram measurements were performed using a PerkinElmer STA8000 simultaneous thermal analyzer. The instrument's temperature sensitivity was calibrated with the melting points of selected pure reference materials under conditions identical to those of the main experiments. An external calibration curve was established by comparing known melting points with measured values for Bi_2O_3 (99.975%), PbO (99.9%), GeO_2 (99.9999%), CuO (99%), MgF_2 (99.9%), $Ca_2P_2O_7$ (99.9%), and $Mg_2P_2O_7$ (99.9%), all sourced from Alfa Aesar. These reference materials cover a temperature range from 1098 to 1668 K, consistent with the STA8000's maximum operating temperature of 1673 K. The root mean square error of the calibration was 7 K. This error range is in agreement with previously reported temperature uncertainties in phase diagram measurements [76, 77].

Several measurements were conducted on the GeO_2–CaO binary system to determine transition temperatures, including solidus and liquidus points. Before each main experiment, baseline correction runs were carried out using the same Pt tube (prior to sample loading) to enhance the accuracy of the DTA curves. This procedure accounted for thermal background contributions from the Pt capsules, alumina crucibles, and carrier gas. During measurements, sealed samples in Pt capsules were placed inside standard alumina crucibles within the STA8000, with an empty alumina crucible used as the reference. To enhance sample homogeneity and reproducibility, each sample underwent at least two heating cycles, with an annealing step (1 h) at subsolidus temperatures between cycles. Thermal profiles and heating rates were optimized based on preliminary experimental results. All measurements were conducted under an inert atmosphere, using a continuous flow of 50 mL/min high-purity Ar (99.999%). Potential mass loss from Pt capsule rupture (often occurring at weld zones) was monitored by TGA during the experiments. Key details of successful measurements in this binary system are summarized in Table 2.

4.3 | Equilibration–Quenching

For static phase diagram measurements, the sample E.D.88G.12C was equilibrated at the target temperature in a Pyradia box furnace, while the E.55G.45C sample was equilibrated at the target temperature in a controlled-atmosphere tube furnace (MTI GSL 1600X-40) and then rapidly quenched in water to preserve high-temperature phase equilibria. In addition to the furnace's built-in thermocouple, the temperature near each sample was continuously monitored using either an Omega K-type thermocouple (KMQXL-125U) or an Omega Pt-30%Rh B-type thermocouple (BAT-QD-ST4-24-18-NHX-M), both positioned horizontally and in direct contact with the sample.

After quenching, samples were removed from their Pt capsules and cold-mounted in epoxy resin. Surface preparation involved successive grinding and polishing steps using lapping oil, with final polishing stages reaching 1 and 0.25 μm diamond lapping pads to avoid water-induced alterations. Initial bulk characterization was carried out using optical microscopy, a Hitachi TM3000 tabletop SEM-EDS (15 kV, 40 nA), and XRD (Anton Paar XRDynamic 500, Cu Kα ~1.5406 Å). Due to the small sample size, fluorescence mapping was employed prior to XRD to precisely optimize beam positioning, ensuring the X-ray beam targeted only the sample surface and avoided the surrounding epoxy. Phase composition was measured using EPMA (JEOL JXA-HP200F) at 15–20 kV accelerating voltage and 20–40 nA beam current. Beam size was carefully optimized through backscattered electron (BSE) imaging and by monitoring elemental mass loss during wavelength-dispersive spectrometry (WDS). After calibrating the WDS detectors, mass loss of Ge and Ca was assessed over a 2-min electron beam interaction. Based on this assessment, a beam diameter of 5 μm was selected as optimal. To minimize electron charging during EPMA analysis, the sample surface was coated with a 20 nm carbon layer before measurement.

The same encapsulated D.88G.12C sample used in the DTA measurements, which exhibited no mass loss, was subsequently utilized for high-temperature equilibration–quenching. This experiment, hereafter referred to as E.D.88G.12C, involved equilibration at 1403 K, above the solidus temperature, within the two-phase region for 48 h, followed by quenching in water. Bulk characterization by SEM and XRD confirmed the presence of a two-phase assemblage.

The second equilibrium–quenching experiment in this system, designated E.55G.45C, was performed at 1622 K for 48 h. During the run, rupture of the Pt capsule weld zone occurred. The resulting microstructure is analyzed and discussed in Section 5.2.2. A summary of the initial conditions for the equilibrium–quenching experiments is provided in Table 3.

5 | Experimental Results

5.1 | Thermal Analysis

This section presents the DTA-TGA results for three samples in the GeO_2–CaO binary system, as listed in Table 2.

15512916, 2026, 2, Downloaded from https://ceramics.onlinelibrary.wiley.com/doi/10.1111/jace.70551 by Ecole De Technologie Superieur, Wiley Online Library on [25/03/2026]. See the Terms and Conditions (https://onlinelibrary.wiley.com/terms-and-conditions) on Wiley Online Library for rules of use; OA articles are governed by the applicable Creative Commons License

TABLE 2 | Initial conditions of DTA-TGA experiments in the GeO_2–CaO binary system.

Sample ID	Composition (mole fraction)	Sample mass (mg)	Heating rate (K/min)	Ar gas flow (mL/min)
D.93G.07C	0.07 CaO	13.3	10	50
D.88G.12C	0.12 CaO	16.4	10	50
D.72G.28C	0.28 CaO	30.4	3	50

TABLE 3 | Initial conditions of equilibration–quenching experiments in the GeO_2–CaO binary system.

Sample ID	Composition (mole fraction)	Mass (mg)	Furnace	External thermocouple	Atmosphere	Sample tray
E.D.88G.12C	0.12 CaO	16.4	Box furnace	K-type	Air	Porous Al_2O_3
E.55G.45C	0.45 CaO	19.4	Tube furnace	B-type	Ar (20 mL/min)	Graphite

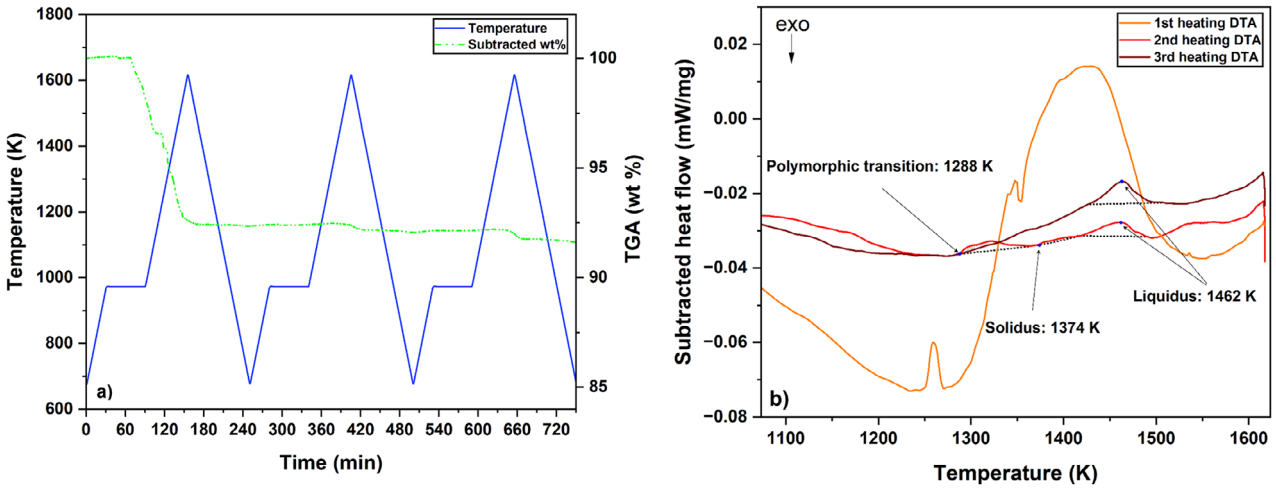

FIGURE 2 | Sample D.93G.07C: (a) thermal profile and TGA results, (b) DTA results.

5.1.1 | D.93G.07C Sample

The sample D.93G.07C underwent three heating cycles, each incorporating a 1-h annealing step at 973 K to enhance homogeneity and facilitate the reverse solid-state transformation of hexagonal GeO_2 to its tetragonal form. Preliminary characterization revealed that the as-received GeO_2 powder predominantly exhibited the high-temperature hexagonal structure (see Figure 1). Inducing this reverse transition was intended to enhance the DTA signal near the polymorphic transformation at 1308 K [22], as previous studies have shown this transition to be extremely sluggish [66] and difficult to detect as a distinct DTA peak.

Due to the high GeO_2 content, the internal vapor pressure within the sealed capsule rose significantly, ultimately causing capsule rupture and mass loss, particularly during the first heating cycle. This was primarily because the sample, still a mechanical mixture of powders at that stage, had not yet undergone melting. The fine particle size further contributed to the volatility of GeO_2, compounding the effects of its inherently high vapor pressure and concentration. The thermal profile and TGA results for this experiment are presented in Figure 2a.

All DTA data were collected during the heating cycles only, as the cooling rate cannot be programmed with the employed DTA instrument and is not constant, particularly in the 1073–1473 K range where most of the system reactions occur. This variability introduces instrumental artifacts that complicate the interpretation. For solid-state transitions, including polymorphic transformations and the solidus temperature, the transition temperatures were determined from the intersection onset of the DTA peaks. The liquidus temperature was taken as the peak maximum, consistent with their thermodynamic definitions [78].

The DTA results for this experiment are presented in Figure 2b. During the first heating cycle, sublimation of solid GeO_2 powders produced a broad, intense peak that overlapped with other thermal events, complicating the identification of individual phase transitions. Once the sample was fully melted and GeO_2 had reacted with CaO, its incorporation into the melt stabilized GeO_2 and lowered its partial pressure over the GeO_2–CaO melt. As a result, mass loss decreased significantly in the second and third heating cycles, enabling clearer observation of phase transitions. However, a slight mass loss was still observed during subsequent heating cycles, as indicated by the TGA results and

15512916, 2026, 2, Downloaded from https://ceramics.onlinelibrary.wiley.com/doi/10.1111/jace.70551 by Ecole De Technologie Superieur, Wiley Online Library on [25/03/2026]. See the Terms and Conditions (https://onlinelibrary.wiley.com/terms-and-conditions) on Wiley Online Library for rules of use; OA articles are governed by the applicable Creative Commons License

TABLE 4 | Summary of DTA results obtained in the GeO_2–CaO system from this work, along with the data reported by the previous work [18, 19].

Sample ID	Initial composition (mole fraction)	Actual composition (mole fraction)	Measured T (K)	
			This work	[18, 19]
D.93G.07C	0.07 CaO	0.08 CaO (first, second, and third)	Second[a]: 1288 K (P.T.)	No P.T. was reported
			Second: 1374 K (solidus)	1403 K
			Second and third: 1462 K (liquidus)	1553 K (monotectic)
D.88G.12C	0.12 CaO	0.12 CaO (first and second)	First: 1309 K (P.T.)	No P.T. was reported
			Second: 1365 K (solidus)	1403 K (solidus)
			First: 1497 (liquidus) Second: 1499 (liquidus)	1553 K (monotectic)
D.72G.28C	0.28 CaO	0.29 CaO (first) 0.3 CaO (second)	First: 1488 (transition) Second: 1489 (transition)	No transition was reported
			First: 1543 (eutectic) Second: 1542 (eutectic)	~1533 K (eutectic)

Abbreviation: P.T., polymorphic transition.

[a]First, second, third = addressing the number of heating cycles.

the broad peak appearing after the liquidus in the second heating cycle. The liquidus temperature was determined to be 1462 K based on the second and third heating cycles.

The reduced peak intensity observed in the third cycle, particularly for the polymorphic transformation and the solidus transition, can be attributed to incomplete recrystallization of the melt upon cooling. A considerable portion of the sample could solidify into a metastable glass, limiting the extent of thermal effect associated with the solid-state transitions in the subsequent heating cycles. The presence of metastable glass upon cooling is a recurring challenge in these experiments [24], as the viscous melt hinders crystal nucleation during the cooling process. Therefore, the solid-state transition temperatures were taken from the second heating cycle.

Mass loss was carefully monitored during each heating cycle to quantify GeO_2 volatilization, and the bulk sample composition was corrected accordingly to ensure accurate positioning on the phase diagram. The corrected values are summarized in Table 4.

5.1.2 | D.88G.12C Sample

Due to the progressive decrease in peak intensity caused by metastable glass formation during cooling, the D.88G.12C sample was subjected to two heating cycles, each reaching the maximum operating temperature of 1673 K. The annealing step and heating rate were identical to those used for sample D.93G.07C. The thermal profile and corresponding TGA results, which confirm the absence of mass loss, are shown in Figure 3a. Transition temperatures were determined using the same criteria as in the previous experiment. The DTA curves from both heating cycles are presented in Figure 3b. In the first heating cycle, the GeO_2 polymorphic transition appeared as a broad, low-intensity peak overlapping with the nearby solidus transition, reflecting the sluggish nature of this transformation, evident from the slow rise and return of the signal to baseline. In the second heating cycle, the polymorphic peak is no longer observed, and only a small solidus peak is observed. This behavior can be attributed to partial recrystallization from the melt and the formation of a metastable glass during cooling, as discussed earlier.

5.1.3 | D.72G.28C Sample

The objective of this experiment was to determine the solidus and liquidus temperatures near 72 mol% GeO_2, for a higher content of CaO, in the GeO_2–CaO phase diagram. Building on previous experiments in this system, the heating rate was reduced from 10 to 3 K/min to possibly minimize the metastable glass content of the sample during the subsequent heating cycle, allowing more time for recrystallization and enhancing the sharpness of thermal peaks. The experiment involved two heating cycles, each including a 1-h annealing step at 1373 K. Despite the lower GeO_2 content in this composition, a higher sample mass of 30.4 mg, sealed in the same capsule size, increased the vapor pressure, resulting in weld rupture and some mass loss during heating. Figure 4a shows the thermal profile and TGA results for the sample D.72G.28C. The apparent exothermic peak at 1373 K is due to the 1-h isothermal hold applied in all DTA measurements (sample-dependent) to improve sample homogeneity prior to the main reactions. Such holds can produce baseline artifacts that appear as peaks.

As with the previously discussed sample, to account for volatilization, the evaporative loss was subtracted from the initial composition, yielding the effective composition at the time of each measurement. This correction ensures that the solidus and liquidus transitions are accurately represented on the phase diagram. The combination of a lower heating rate and higher sample mass significantly improved signal quality, making it easier to identify individual transition peaks. A transition peak and a eutectic peak were identified at 1488 and 1543 K during the first heating cycle, and at 1489 and 1542 K during the second heating cycle, respectively. The eutectic reaction corresponds to

15512916, 2026, 2, Downloaded from https://ceramics.onlinelibrary.wiley.com/doi/10.1111/jace.70551 by Ecole De Technologie Superieur, Wiley Online Library on [25/03/2026]. See the Terms and Conditions (https://onlinelibrary.wiley.com/terms-and-conditions) on Wiley Online Library for rules of use; OA articles are governed by the applicable Creative Commons License

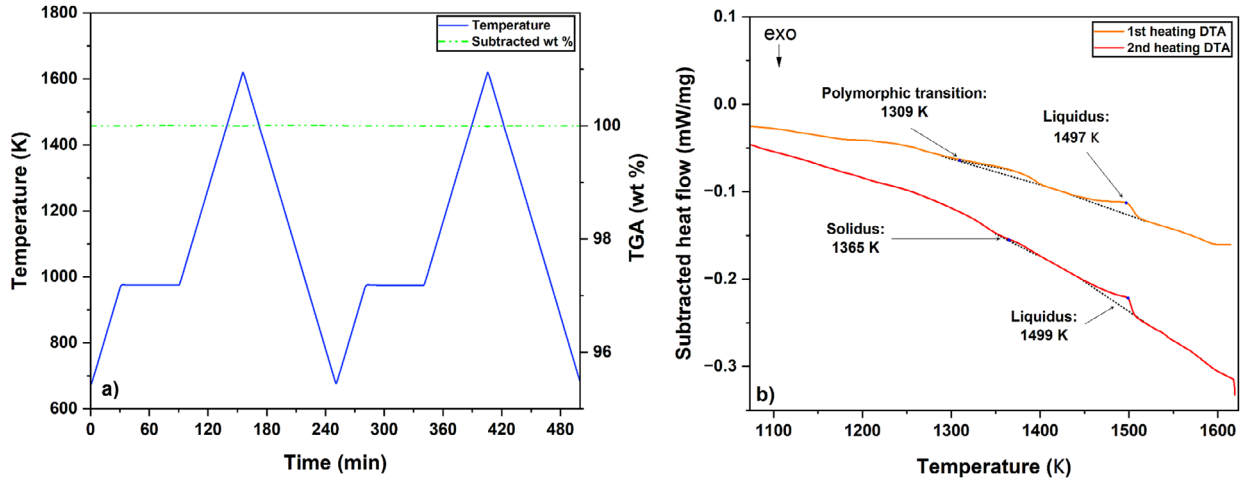

FIGURE 3 | Sample D.88G.12C: (a) thermal profiles and TGA results, (b) DTA results.

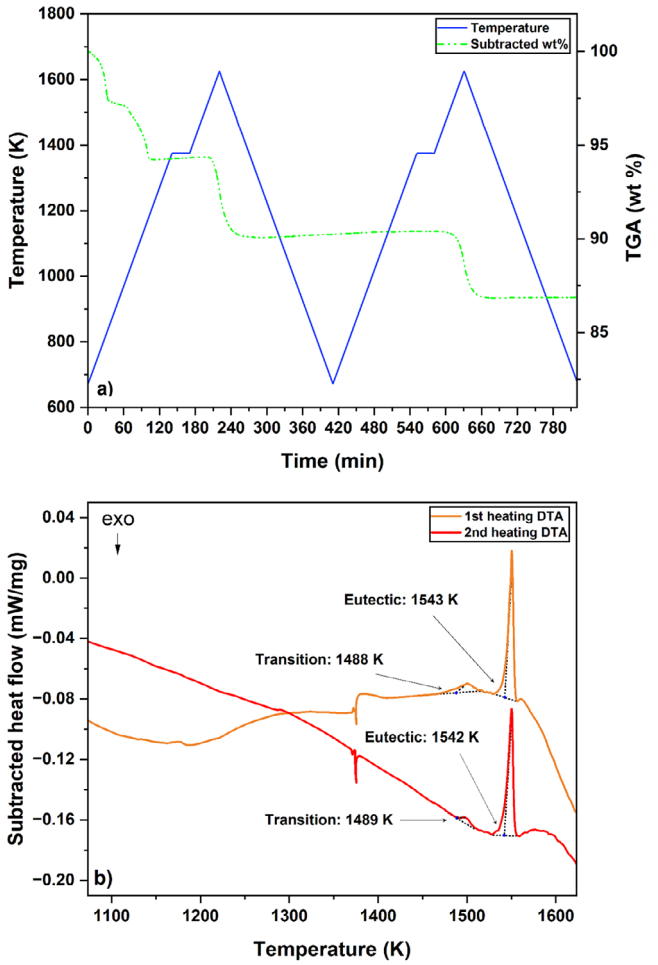

FIGURE 4 | Sample D.72G.28C: (a) thermal profile and TGA results, (b) DTA results.

L → $Ca_2Ge_7O_{16}$ + $CaGe_2O_5$ (~30 mol% CaO, ~1542 K). The first peak (onset at 1488 and 1489 K) is interpreted as a transition peak, possibly associated with a polymorphic transformation of one of the compounds, which warrants further investigation. The DTA curve and the corresponding transition temperatures are presented in Figure 4b.

Table 4 summarizes the DTA results obtained for the GeO_2–CaO binary system in this work, along with the data reported by Shirvinskaya et al. [18] and Grebenshcikov et al. [19]. We have corrected the bulk nominal compositions of the samples experimented in this work for GeO_2 mass loss based on the TGA results. Our experimental data on the GeO_2-rich side of the phase diagram show good internal consistency. The liquidus temperatures were reproduced very consistently across the samples in the GeO_2-rich region, with a maximum variation of ± 2 K. A deviation of approximately 9 K is observed in the solidus temperature on the GeO_2-rich side (between samples D.93G.07C and D.88G.12C), while it remains within the acceptable range of experimental error. The eutectic temperature of sample D.72G.28C was reproduced within ± 1 K. A difference of ~21 K is noted in the polymorphic transition temperatures between samples D.93G.07C (1288 K) and D.88G.12C (1309 K); however, this transition has also been reported in the literature at temperatures ranging from 1281 K [21] to 1310 K [22]. This discrepancy likely arises from kinetic barriers associated with the transition, making it difficult to reproduce identical results across different measurements. Sarver and Hummel [79] and Yonemura and Kotera [21] reported that this phase transformation is sluggish and can be facilitated by the presence of catalysts such as alkali oxides, halides, or the application of high pressure. Yonemura and Kotera [21] reported that the intermediate phase $Li_2O{\cdot}7GeO_2$, which forms below the temperature of the GeO_2 polymorphic transition, plays a catalytic role in the tetragonal-to-hexagonal transformation. By analogy, we speculate that a similar mechanism could occur in the GeO_2–CaO system. The formation of $2CaO{\cdot}7GeO_2$ ($Ca_2Ge_7O_{16}$, analogous to $Li_2O{\cdot}7GeO_2$) during the second heating cycle may act as a catalytic intermediate, facilitating the phase transformation, and lowering the transition temperature from 1309 K (the first heating cycle) to 1288 K (the second heating cycle). However, the identification of this intermediate phase and confirmation of its catalytic role were beyond the scope of this study, and need to be further investigated. The solidus temperatures in the GeO_2-rich region reported by the previous group [18, 19] are systematically higher than those measured in the present work. They exceed our measurements by 29–38 K. The β-quartz GeO_2 was also reported to melt at 1409 K, which is higher than both the values reported in an earlier study (1388 K) [79] and the melting point from the current thermodynamic optimization

15512916, 2026, 2, Downloaded from https://ceramics.onlinelibrary.wiley.com/doi/10.1111/jace.70551 by Ecole De Technologie Superieur, Wiley Online Library on [25/03/2026]. See the Terms and Conditions (https://onlinelibrary.wiley.com/terms-and-conditions) on Wiley Online Library for rules of use; OA articles are governed by the applicable Creative Commons License

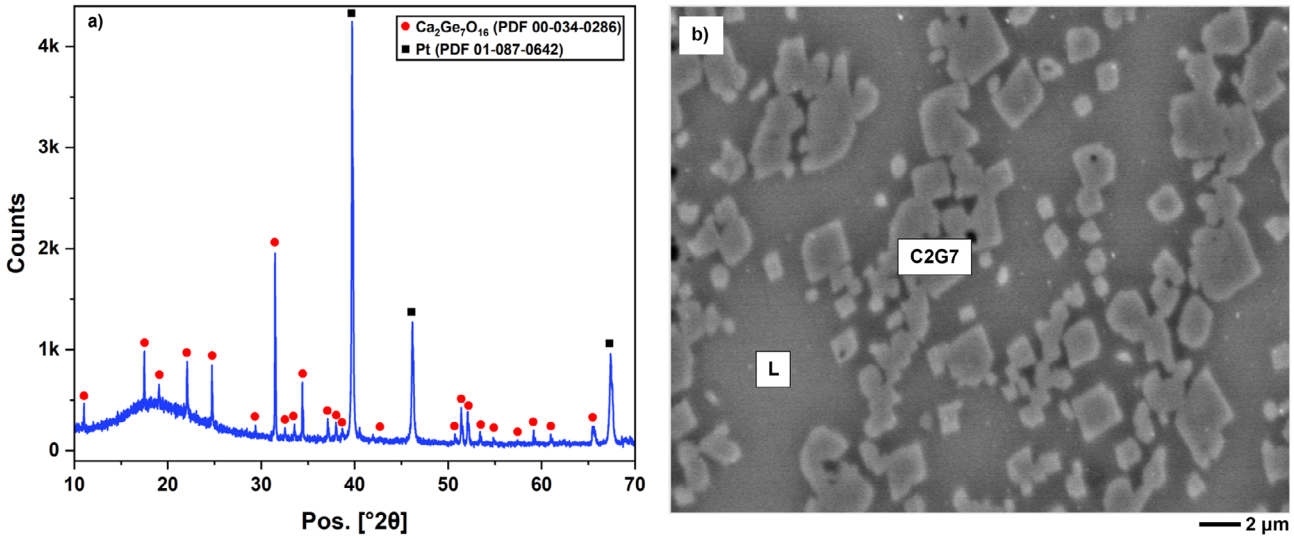

FIGURE 5 | Sample E.D.88G.12C after equilibration–quenching at 1403 K for 48 h: (a) XRD, (b) BSE image. C2G7, $Ca_2Ge_7O_{16}$; L, liquid.

(1397 K). This discrepancy may be attributed to kinetic effects, where higher heating rates in thermal analysis are known to shift transition temperatures to higher values. Additionally, in our study, both calibration and correction runs were performed to improve the accuracy of the measurements, as detailed in Section 4. Moreover, we did not observe any monotectic transitions on the GeO_2-rich side of the diagram, which is consistent with the results of our equilibration–quenching tests, as discussed in Section 5.2. The eutectic point, measured at ~30 mol% CaO and ~1542 K [18, 19], shows good agreement with earlier determinations at 31 mol% CaO and ~1533 K. The data obtained in this study were used for thermodynamic modeling.

5.2 | Equilibration–Quenching

All phase equilibrium data, microstructural characterizations, and phase identifications related to equilibrium–quenching experiments are discussed in this section.

5.2.1 | E.D.88G.12C

Sample D.88G.12C was heated to 1403 K, approximately 30 K above its solidus temperature, and held for 48 h to validate the solidus temperature previously determined by DTA (see Table 4) and to confirm the stoichiometry of the binary compound. Figure 5a presents the XRD pattern of sample D.88G.12C after equilibration–quenching.

XRD analysis revealed the presence of two distinct phases in the sample. A broad hump at low angles indicates the presence of an amorphous phase, corresponding to liquid at high temperature. In addition, the sharp diffraction peaks were indexed to $Ca_2Ge_7O_{16}$ (PDF 00-034-0286), while the Pt peaks observed originate from the capsule used to contain the mixture. These results confirm the formation of the $Ca_2Ge_7O_{16}$ compound under equilibrium conditions, in agreement with the recent study by Redhammer et al. [61]. Consequently, the previously proposed compound $CaGe_4O_9$, reported by Shirvinskaya et al. [18] and Grebenshchikov et al. [19], is revised to $Ca_2Ge_7O_{16}$ in this study for final thermodynamic optimization of the GeO_2–CaO phase diagram. The BSE image in Figure 5b clearly illustrates the distribution of stoichiometric $Ca_2Ge_7O_{16}$ crystals embedded within the surrounding liquid matrix. The chemical compositions of both crystalline and liquid phases were determined by EPMA, with 10 randomly selected spectra collected for each phase. Table 5 summarizes the experimental conditions, the identified equilibrium phases, and their corresponding compositions.

The quantification of the liquidus composition for this sample, along with the previously discussed DTA measurements for samples D.93G.07C and D.88G.12C, reveals a consistent and gradual decrease in liquidus temperature approaching the eutectic point. This trend contrasts with the findings of Shirvinskaya et al. [18] and Grebenshchikov et al. [19], who proposed the presence of a miscibility gap in this compositional region. No indication of a monotectic isotherm was observed in the measurements conducted in the present study. Due to the limited experimental details reported by Grebenshchikov et al. [19], it is difficult to critically assess their data. One plausible explanation for the observed miscibility gap in their study could be the presence of carbonate impurities, as their samples were prepared using $CaCO_3$ as a starting material, unlike the present study, which employed high-purity CaO powders subjected to a drying pretreatment prior to sample preparation. The formation of miscibility gaps induced by carbonate species in similar silicate melts has been discussed by Brooker and Kjarsgaard [80]. Additionally, the miscibility gap reported in the GeO_2–CaO system expands over a rather narrow compositional range (86–96 mol% GeO_2), compared to the broader gap reported in the CaO–SiO_2 and MgO–GeO_2 systems, which extend nearly across the entire SiO_2- or GeO_2-rich side. While the CaO–SiO_2 and MgO–GeO_2 systems display wide miscibility gaps and lack stoichiometric compounds on the silica- or germania-rich side, the GeO_2–CaO system contrasts by featuring two congruently melting calcium germanates in the GeO_2-rich region, suggesting strong chemical interactions between CaO and GeO_2. This behavior appears inconsistent with the existence of a miscibility gap, which typically reflects positive deviations from ideal mixing. Additionally, on the

15512916, 2026, 2, Downloaded from https://ceramics.onlinelibrary.wiley.com/doi/10.1111/jace.70551 by Ecole De Technologie Superieur, Wiley Online Library on [25/03/2026]. See the Terms and Conditions (https://onlinelibrary.wiley.com/terms-and-conditions) on Wiley Online Library for rules of use; OA articles are governed by the applicable Creative Commons License

TABLE 5 | Experimental results of equilibrium–quenching tests in the GeO_2–CaO system.

Sample ID	Detected mass loss (mg)	Composition after detected mass loss (mole fraction)	Experiment conditions	Identified phases (XRD or SEM)	Composition (EPMA)		
					# of analysis	CaO mole fraction ± 1σ	GeO_2 mole fraction ± 1σ
E.D.88G.12C	—	0.12 CaO	1403 K 48 h	$Ca_2Ge_7O_{16}$	10	0.229 ± 0.011	0.771 ± 0.011
				Liquid	10	0.068 ± 0.003	0.932 ± 0.003
E.55G.45C[a]	3.7	0.53 CaO	1622 K 48 h	Acicular $CaGeO_3$	N/A	—	—
				Prismatic Ca_2GeO_4	8	0.680 ± 0.001	0.320 ± 0.001
				Heterogenous liquid	N/A	—	—

[a]Equilibrium was not achieved.

GeO_2-rich side, calcium digermanates and tetragermanates resemble titanates and benitoite-type structures [19, 56, 81], whereas those on the CaO-rich side resemble silicate analogues with predominant olivine- and wollastonite-type structures. This might imply a compositional transition in behavior from silicate-type to titanosilicate-type compounds across the system, and no miscibility gap has also been reported for the CaO-TiO_2 system. Furthermore, the equilibration time used in the previous experiments [18, 19] was not reported. Given the known viscous behavior of GeO_2, extended equilibration times are necessary to achieve complete phase separation. In the present study, even after 48 h of equilibration at 1408 K for sample D.88G.12C, the small crystal size suggests that nucleation and growth of the solid phase were still at an early stage. This suggests that insufficient equilibration time could have also contributed to the apparent miscibility gap reported by the previous group.

5.2.2 | E.55G.45C

The experiment on the E.55G.45C sample was performed at 1622 K for 48 h to achieve equilibrium between the liquid phase and solid $CaGeO_3$, aiming to precisely quantify the liquidus composition and better approximate the temperature and composition of the eutectic reaction in this region (Liquid → $CaGeO_3$(s) + $CaGe_2O_5$(s)). However, a mass loss of 3.7 mg, attributed to GeO_2 volatilization, was observed between the initial and final sample masses (including drying), shifting the composition from 45 to 53 mol% CaO on the phase diagram. Upon opening the capsule, the sample appeared sintered with an unexpected light-blue color instead of white. SEM imaging of the as-quenched and as-polished samples, as shown in Figure 6, revealed three main phases: prismatic crystals and acicular/fibrous crystals distributed along the rim in contact with a heterogeneous liquid matrix. According to the Gibbs phase rule, three-phase equilibrium is possible only at the eutectic invariant temperature. Given the low likelihood that the experimental temperature matched this exactly, the sample probably did not reach global equilibrium. The observed microstructure indicates a two-phase assemblage, with acicular crystals in contact with the liquid and prismatic crystals developing from them during isothermal heating. The observed blue coloration could be related to quantum size effects in the nanofibers, which lead to band gap widening and consequently alter their light absorption and emission properties [82].

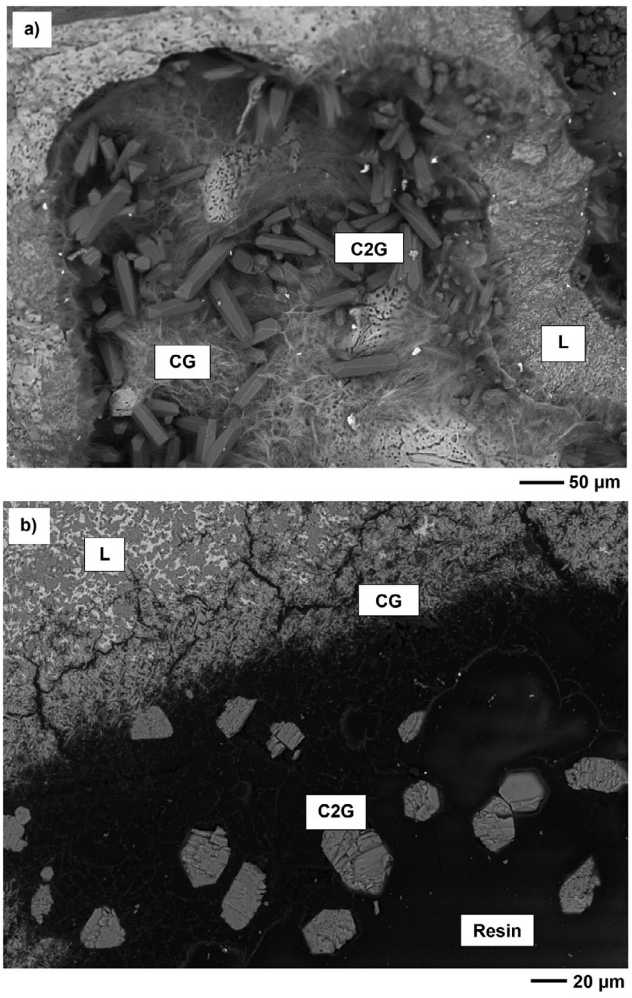

FIGURE 6 | BSE-SEM images of sample E.55G.45C after equilibration–quenching at 1622 K for 48 h: (a) as quenched, (b) as polished. C2G, Ca_2GeO_4; CG, $CaGeO_3$; L, liquid.

XRD of the as-quenched sample shown in Figure 7 identifies $CaGeO_3$ (acicular/fibrous) and Ca_2GeO_4 (prismatic), while $Ca_3Ge_2O_7$ is absent. This absence is likely due to progressive GeO_2 evaporation, which would shift the composition toward a phase with lower GeO_2 content, namely, Ca_2GeO_4. It should also be noted that the actual mass loss was likely greater than the reported 3.7 mg, as Ge-bearing species condensed on the

15512916, 2026, 2, Downloaded from https://ceramics.onlinelibrary.wiley.com/doi/10.1111/jace.70551 by Ecole De Technologie Superieur, Wiley Online Library on [25/03/2026]. See the Terms and Conditions (https://onlinelibrary.wiley.com/terms-and-conditions) on Wiley Online Library for rules of use; OA articles are governed by the applicable Creative Commons License

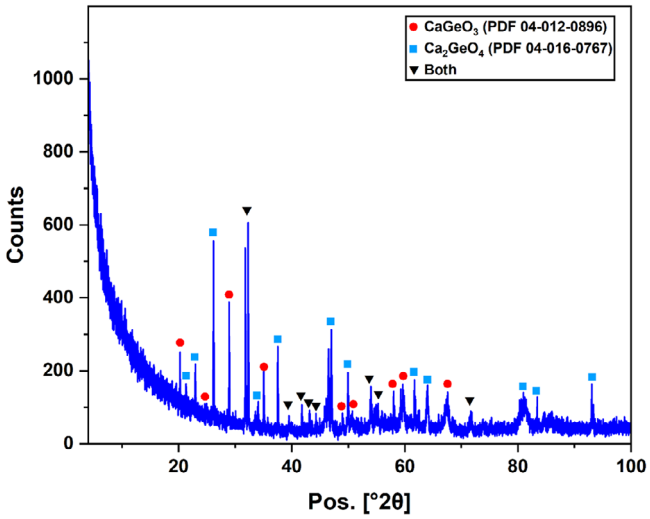

FIGURE 7 | XRD analysis of sample E.55G.45C after equilibration–quenching at 1622 K for 48 h.

inner walls of the Pt capsule and would not be reflected in the recorded mass difference before and after the experiment. SEM-EDS elemental mapping of the polished sample depicted in Figure 8 reveals a liquid phase with nonuniform composition that remained from the targeted stability region (i.e., 45 mol% CaO), reflecting partial GeO_2 loss and compositional shifts during the experiment.

Eight well-grown prismatic crystals were analyzed by EPMA to determine their chemical composition. The results confirmed that the prismatic crystals correspond to Ca_2GeO_4, consistent with the XRD findings. The liquid matrix could not be reliably analyzed due to its heterogeneity, and the data were very scattered. Because the experiment was affected by capsule rupture and mass loss, the results were intended for qualitative interpretation of phase equilibria rather than quantitative determination of phase boundaries. The microstructural evidence implies that the E.55G.45C sample, originally containing 45 mol% CaO, lies within the two-phase region consisting of liquid and $CaGeO_3$ at 1622 K, and supports the stability of Ca_2GeO_4 at higher CaO concentrations at 1622 K. These observations are consistent with the data previously reported by Shirvinskaya et al. [18]. Table 5 summarizes the results of the equilibrium–quenching experiments in the GeO_2–CaO system.

6 | Thermodynamic Optimization

6.1 | Unary Oxides

Based on a critical assessment of available literature data and the new experimental data obtained in this study, the model parameters of the proposed thermodynamic models were optimized to reproduce all reliable thermodynamic properties and phase diagram data within experimental error margins. Table 6 presents the optimized thermodynamic properties of pure GeO_2 and pure CaO. Figure 9 shows the calculated C_p of the two GeO_2 polymorphs and the glass–liquid phase, alongside the corresponding experimental data.

The experimental equilibrium constant of reaction (1) in the temperature range of 1250–1370 K was calculated using the data reported by Smirnov et al. [34], according to the following reaction:

$$K = p_{GeO} \cdot {p_{O_2}}^{0.5} / a_{GeO_2}, \tag{13}$$

where p_i is the partial pressure of gaseous species, and a_{GeO_2} is the activity of pure solid GeO_2, which is 1.0. In addition, the equilibrium constant for the same reaction was calculated using the thermodynamic properties of solid GeO_2 optimized in this work and the gaseous species, that is, GeO(g) and O_2(g), partial pressures taken from FactSage 8.2 FactPS database. Figure 10 compares the calculated equilibrium constant of solid GeO_2 sublimation and the experimental data.

The slope of this graph represents the enthalpy of sublimation of GeO_2(s):

$$ln\,(K) = -\Delta H_{rxn}/R \cdot 1/T + \Delta S_{rxn}/R, \tag{14}$$

where $R = 8.314$ J/mol·K is the universal gas constant, T is the temperature in K, and ΔH_{rxn} and ΔS_{rxn} represent the enthalpy and entropy of the reaction, respectively. Based on the present calculations, the enthalpy of the $GeO_{2(Hex.)}$ evaporation reaction at 298.15 K is estimated at 510.860 kJ/mol, which is in acceptable agreement with the value of 514 ± 18.2 kJ/mol derived from the data of Smirnov et al. [34].

6.2 | Binary Systems

For Ca_3GeO_5, several polymorphs and their transition temperatures have been reported based on high-temperature XRD studies [19, 52]. However, as no enthalpy or entropy data for these transitions are available, these compounds were treated as single-polymorph phases in the present optimization.

The thermodynamic properties of the stoichiometric compounds in the GeO_2–CaO binary system are summarized in Table 7. Figure 11 displays the calculated C_p of Ca_2GeO_4, along with the corresponding experimental data from low temperatures and the Neumann–Kopp rule (NKR) estimation. The C_p values of the other binary compounds were estimated by summing the C_p of the constituent oxides, GeO_2 (hexagonal) and CaO, based on their stoichiometric molar ratios. Since no direct thermodynamic data exist for most Ca-germanates, except for the low-temperature calorimetry of Ca_2GeO_4, the optimization was carried out by balancing constraints from NKR estimations and the liquid mixing energies of analogous systems such as CaO–SiO_2 and CaO–TiO_2, while respecting the reported phase equilibrium data. The resulting model reasonably reproduces the known melting behavior and phase equilibria, with $\Delta H^o_{298\ K}$ and $S^o_{298\ K}$ differences with the corresponding NKR values (3–7% and 0–4%, respectively) falling within the general experimental–NKR deviation ranges reported for similar oxide systems [84], thereby confirming the reliability of the optimization approach considering the limited thermodynamic data available for Ca-germanates.

15512916, 2026, 2, Downloaded from https://ceramics.onlinelibrary.wiley.com/doi/10.1111/jace.70551 by Ecole De Technologie Superieur, Wiley Online Library on [25/03/2026]. See the Terms and Conditions (https://onlinelibrary.wiley.com/terms-and-conditions) on Wiley Online Library for rules of use; OA articles are governed by the applicable Creative Commons License

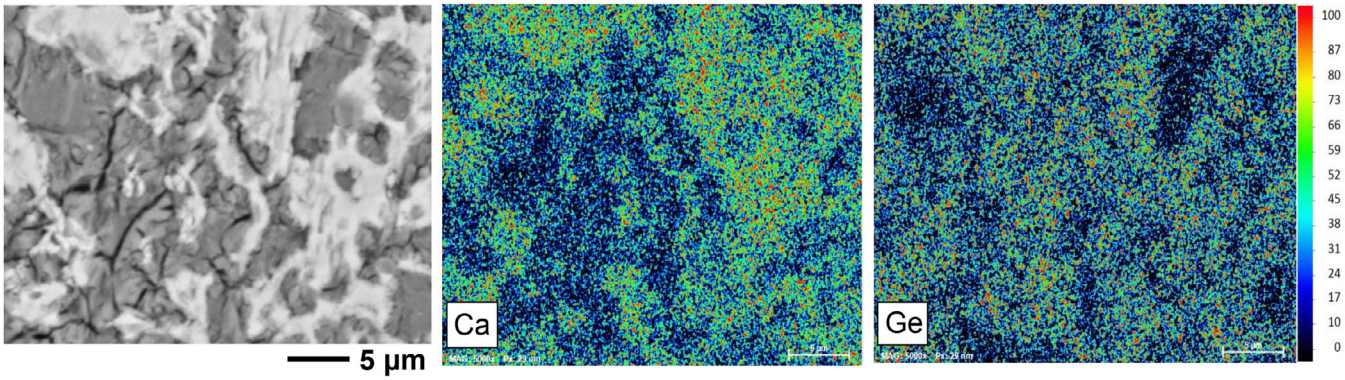

FIGURE 8 | SEM-EDS elemental mapping of the liquid matrix in sample E.55G.45C (as-polished).

TABLE 6 | Thermodynamic properties of unary oxides.

		$\Delta H^{o}_{f,298.15\ K}$ (kJ/mol)	$S^{o}_{298.15\ K}$ (J/mol.k)	C_p (J/mol.K)	Tech.[a]	Ref.
GeO_2	Tet.	−580.20	—		F.C.	[25, 83]
		—	39.710		A.C.	[25, 26]
				$C_p = 68.850 + 0.009 \cdot T - 1903290.560 \cdot T^{-2} - 1.015E - 9 \cdot T^2$ (298.15–1308 K)		This work
	Hex.	—	—	$C_p = 62.208 + 0.014 \cdot T - 1276500 \cdot T^{-2}$ (298.15–800 K)		This work
				$C_p = 108.780 - 0.037 \cdot T - 9999999.90 \cdot T^{-2} + 1.295E - 5 \cdot T^2$ (800–1388 K)		This work
	Trans.	Tet. → Hex. $\Delta H_{T,\ 1308\ K} = 21.50$ (kJ/mol)			DTA	[22]
	Liquid			$C_p = 55.752 + 0.029 \cdot T - 1029769.720 \cdot T^{-2} - 9.030E - 6 \cdot T^2$ (298.15–1400 K) $C_p = 98.889 - 0.021 \cdot T - 9999999.90 \cdot T^{-2} - 7.031E - 6 \cdot T^2$ (1400–2000 K)		This work
		Hex. → Liq. $\Delta H_{T,1388\ K} = 17.20$ (kJ/mol)			DTA	[22, 25]
CaO[a]	Solid	−635.090	37.750	$C_p = 58.791 - 1147145.982 \cdot T^{-2} - 133.904 \cdot T^{-0.5} + 102978787.864 \cdot T^{-3}$ (298.15–3200 K)	Mod.	FToxid
	Liquid	Sol. → Liq. $\Delta H_{T,3200\ K} = 79.50$ (kJ/mol)		$C_p = 62.760$ (3200–3500 K)	Mod.	FToxid
					Mod.	[50]

Note: The thermodynamic properties have been rounded to three decimal places.

Abbreviations: A.C., adiabatic calorimetry; DTA, differential thermal analysis; F.C., fluorine bomb calorimetry; Mod., modeling.

[a]The melting temperature of CaO was re-evaluated and optimized at 3200 K in this work, and based on this value, the thermodynamic properties of the liquid phase were calculated.

Figure 12a,b illustrates the heat content ($H_{973\ K} - H_{298.15\ K}$) and the heat of solution ($H_{\ Liquid,\ 973\ K} - H_{Solids,\ 973\ K}$) for the GeO_2–SiO_2 glass, calculated from the present database along with experimental data. The heat of solution was calculated relative to the crystalline phases: high-temperature quartz and tetragonal GeO_2, to be consistent with the reported experimental data. The calculated heats show fair agreement with the experimental data reported by Maniar et al. [68]. In Figure 12b, the slight deviation between the experimental ideal line and the calculated ideal line may result from minor reactions between

15512916, 2026, 2, Downloaded from https://ceramics.onlinelibrary.wiley.com/doi/10.1111/jace.70551 by Ecole De Technologie Superieur, Wiley Online Library on [25/03/2026]. See the Terms and Conditions (https://onlinelibrary.wiley.com/terms-and-conditions) on Wiley Online Library for rules of use; OA articles are governed by the applicable Creative Commons License

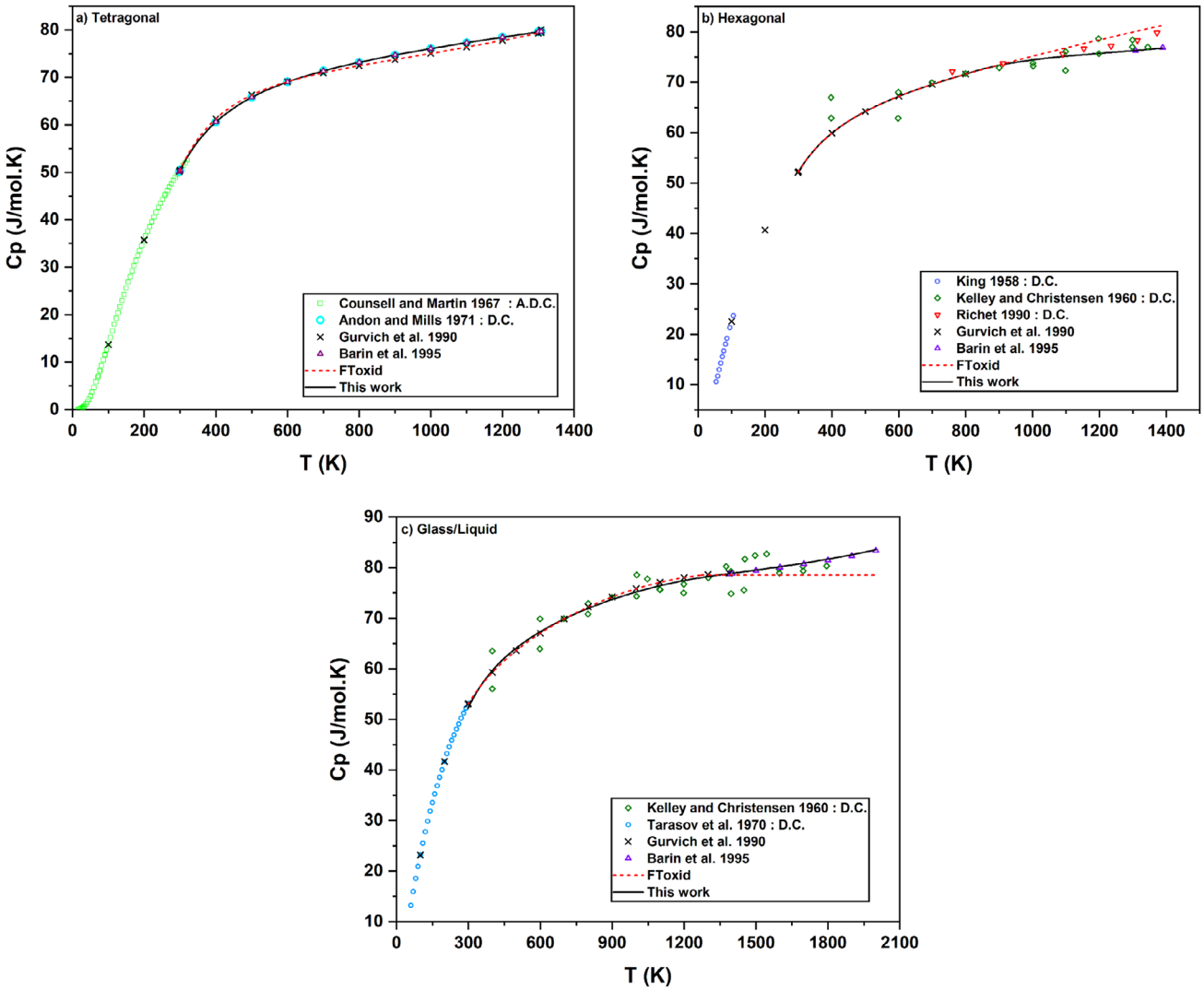

FIGURE 9 | Calculated heat capacity of pure GeO_2 from this study, along with experimental data: (a) tetragonal, (b) hexagonal, (c) glass/liquid. A.D.C., adiabatic drop calorimetry; D.C., drop calorimetry.

TABLE 7 | Thermodynamic properties of stoichiometric compounds in the GeO_2–CaO binary system.

Compound	$\Delta H^o_{f,298.15\ K}$ (kJ/mol)	$S^o_{298.15\ K}$ (J/mol.k)	C_P (J/mol.K)	Tech.[a]	Ref.
Ca_3GeO_5	−2546.650	199.599	$C_p = 3C_p\,(CaO)+C_p\,(GeO_{2\,(Hex.)})$		This work
Ca_2GeO_4		132.055		C	[63]
	−1944.50	133.67	$C_p = 168.071 + 0.037 \cdot T - 3789979.16 \cdot T^{-2} - 6.325E-6 \cdot T^2$ [a] (298 −2200 K)		This work
$Ca_3Ge_2O_7$	−3230.971	235.50	$C_p = 3C_p\,(CaO) + 2C_p\,(GeO_{2\,(Hex.)})$		This work
$CaGeO_3$	−1275.10	100.0	$C_p = C_p\,(CaO)+C_p\,(GeO_{2\,(Hex.)})$		This work
$CaGe_2O_5$	−1850.0	158.50	$C_p = C_p\,(CaO) + 2C_p\,(GeO_{2\,(Hex.)})$		This work
$Ca_2Ge_7O_{16}$	−5424.0	482.0	$C_p = 2C_p\,(CaO) + 7C_p\,(GeO_{2\,(Hex.)})$		This work

Abbreviation: C, calorimetry.

[a]C_p values have been rounded to three decimal places.

15512916, 2026, 2, Downloaded from https://ceramics.onlinelibrary.wiley.com/doi/10.1111/jace.70551 by Ecole De Technologie Superieur, Wiley Online Library on [25/03/2026]. See the Terms and Conditions (https://onlinelibrary.wiley.com/terms-and-conditions) on Wiley Online Library for rules of use; OA articles are governed by the applicable Creative Commons License

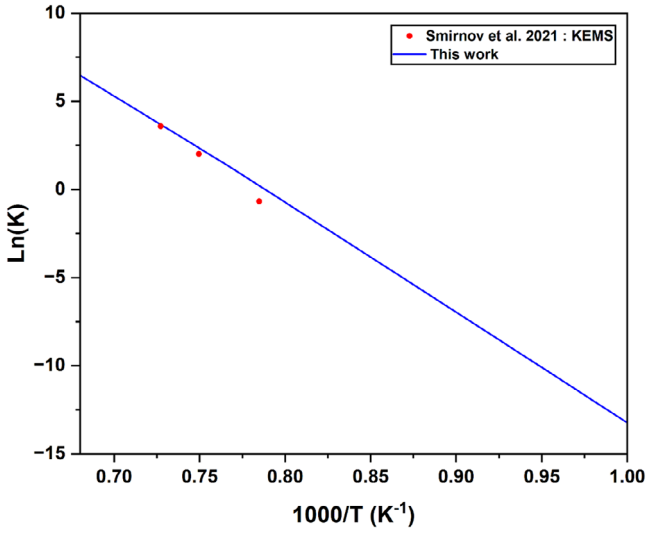

FIGURE 10 | Calculated equilibrium constant of solid GeO_2 sublimation, along with the experimental data.

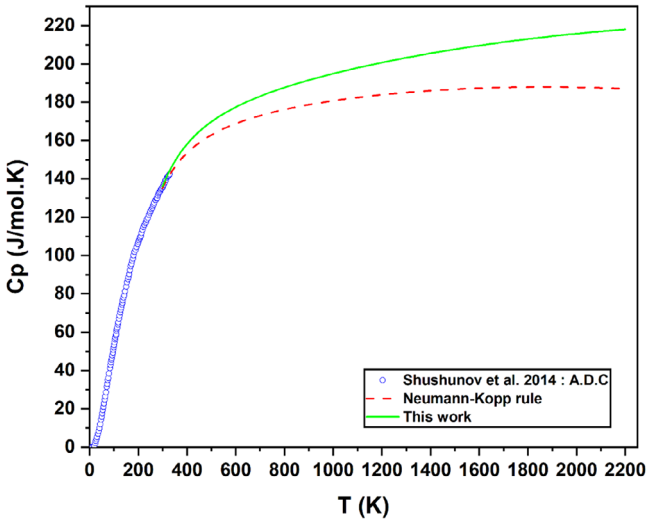

FIGURE 11 | Calculated heat capacity of Ca_2GeO_4, along with the experimental data and NKR estimation. A.D.C., adiabatic drop calorimetry.

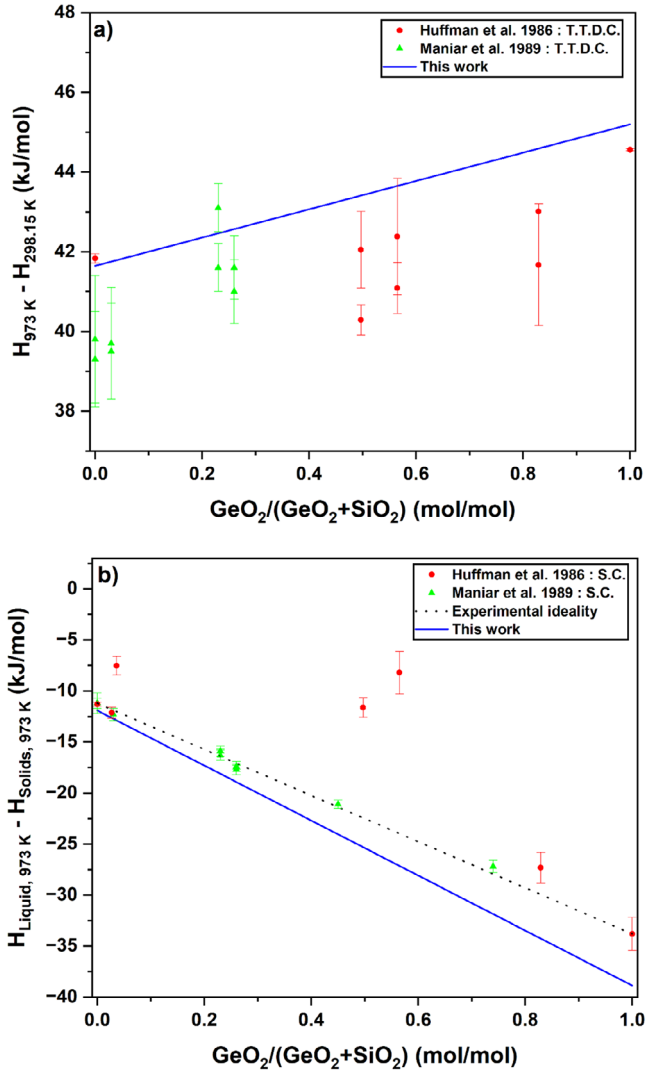

FIGURE 12 | Calculated (a) $H_{973\,K}$-$H_{298.15\,K}$ (heat content) and (b) $H_{Liquid,973\,K} - H_{Solids,973\,K}$ (heat of solution relative to the crystalline phases: quartz [h-T] and GeO_2 [tetragonal]), for the GeO_2–SiO_2 glass, along with the experimental data. h-T, high-temperature; S.C., solution calorimetry; T.T.D.C., transposed temperature drop calorimetry.

the solvent ($2PbO{\cdot}B_2O_3$) and the GeO_2 sample during solution calorimetry, contributing a small amount of additional heat. The thermodynamic data for pure GeO_2 were optimized in this work using experimental results obtained from drop calorimetry in an inert medium, involving no solution and additional reactions, which is considered to be more accurate than the data from solution calorimetry, as detailed in Sections 2.1.1 and 6.1.

The model parameters for the GeO_2–CaO liquid solution and the quartz solid solution in the GeO_2–SiO_2 system, optimized in the current work to reproduce the phase diagram data, are presented in Table 8. The GeO_2–SiO_2 liquid solution was treated as ideal, with $\Delta g_{AB} = 0$.

According to the CALPHAD approach, a phase diagram is the most complete manifestation for showing the thermodynamic assessment of a system. Optimized, calculated phase diagrams related to the GeO_2–CaO and GeO_2–SiO_2 systems are presented in Figures 13 and 14, respectively, along with experimental data from the literature and from this work. Most of the reliable phase diagram data were reproduced within ±50 K. The calculated invariant reactions for both phase diagrams are also listed in Table 9.

7 | Conclusion

This work provides the first comprehensive thermodynamic description of the GeO_2–CaO system based on combined experimental measurements and CALPHAD modeling, along with a reoptimization of the GeO_2–SiO_2 system to ensure internal consistency and improved agreement with reliable literature data. All available thermodynamic property and phase diagram data for the GeO_2–CaO and GeO_2–SiO_2 systems at 1 atm total

15512916, 2026, 2, Downloaded from https://ceramics.onlinelibrary.wiley.com/doi/10.1111/jace.70551 by Ecole De Technologie Superieur, Wiley Online Library on [25/03/2026]. See the Terms and Conditions (https://onlinelibrary.wiley.com/terms-and-conditions) on Wiley Online Library for rules of use; OA articles are governed by the applicable Creative Commons License

TABLE 8 | Optimized model parameters of solutions in the GeO_2–CaO and GeO_2–SiO_2 binary systems.

Solution	System	Thermodynamic model	Model parameters (J/mol)	Ref.
Liquid solution	GeO_2–CaO	MQM	$\Delta g^0_{Ge,Ca} = -170\,000 + 19 \cdot T$ $g^{01}_{Ge,Ca} = -30\,000$ $g^{02}_{Ge,Ca} = -80\,000$ $g^{10}_{Ge,Ca} = -62\,000$ $g^{90}_{Ge,Ca} = 20\,000 - 9.732 \cdot T$	This work
	GeO_2–SiO_2	Ideal	$\Delta g_{AB} = 0$	[66]
Solid solution	Quartz	CEF	$G_{GeO_2} = G^0_{GeO_2(hex.)}$ $G_{SiO_2} = G^0_{SiO_2(hex.)}$ ${}^0L_{Ge,Si} = 3694$ ${}^1L_{Ge,Si} = -2100$	This work FToxid This work

Note: Coordination numbers: $Z^{Ca}_{Ca\,Ca} = 1.3774$ $Z^{Ge}_{Ge\,Ge} = 2.7548$ $Z^{Si}_{Si\,Si} = 2.7548$.

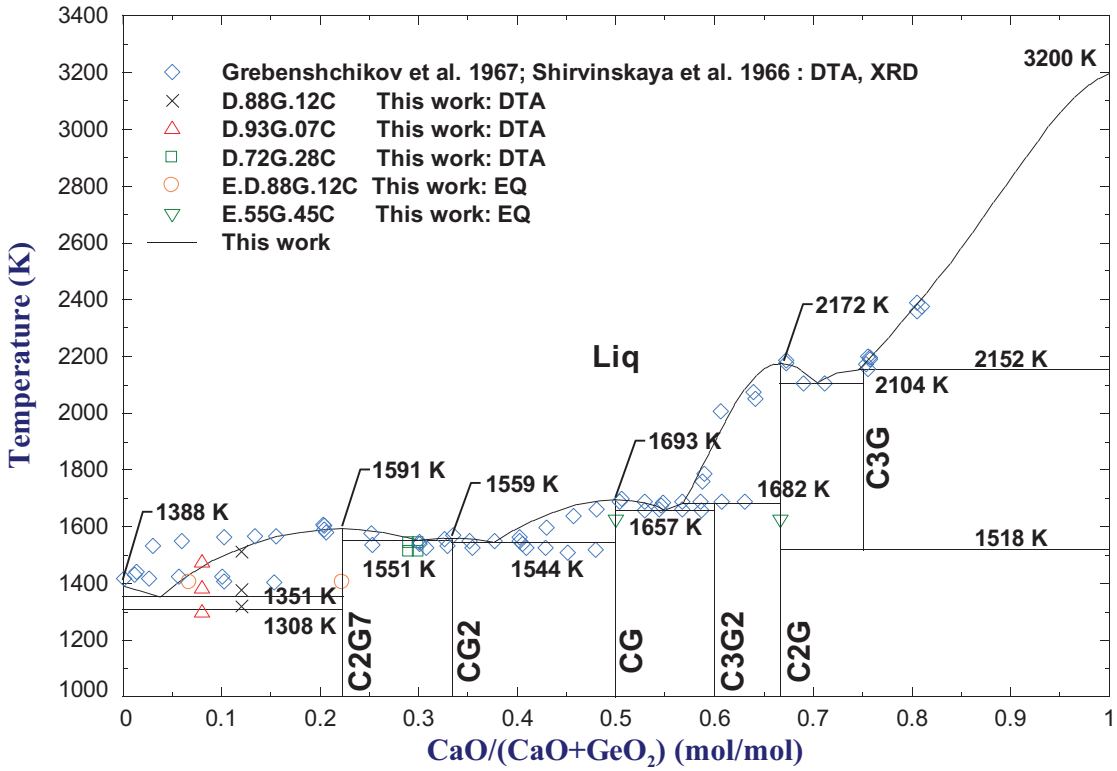

FIGURE 13 | Optimized calculated phase diagram of the GeO_2–CaO binary system, along with the experimental data. Liq, C2G7, CG2, CG, C3G2, C2G, and C3G represent liquid, $Ca_2Ge_7O_{16}$, $CaGe_2O_5$, $CaGeO_3$, $Ca_3Ge_2O_7$, Ca_2GeO_4, and Ca_3GeO_5, respectively.

pressure were critically evaluated and optimized to obtain a self-consistent set of Gibbs energy functions for all stable phases. Discrepancies among previously reported data were resolved, and most of the reliable phase equilibria were reproduced within ±50 K.

New phase diagram measurements for the GeO_2–CaO system were carried out using DTA–TGA and the equilibration–quenching technique in sealed Pt capsules, followed by XRD and EPMA. The results confirm that the phase previously reported as $CaGe_4O_9$ corresponds to $Ca_2Ge_7O_{16}$ under equilibrium conditions and that a eutectic reaction occurs on the GeO_2-rich side, in contrast with earlier studies. The heat capacity of GeO_2 was re-evaluated and reoptimized with respect to the previous optimization, leading to updated C_p expressions and Gibbs energy functions for the solid and liquid phases.

The optimized database developed in this work enables accurate calculation of phase equilibria across wide composition and temperature ranges in the studied systems. Additionally, activities, partial pressures, and other thermodynamic properties can be estimated using the current database. The established database and its models lay the groundwork for future extensions to GeO_2–CaO–SiO_2 ternary and multicomponent oxide systems,

15512916, 2026, 2, Downloaded from https://ceramics.onlinelibrary.wiley.com/doi/10.1111/jace.70551 by Ecole De Technologie Superieur, Wiley Online Library on [25/03/2026]. See the Terms and Conditions (https://onlinelibrary.wiley.com/terms-and-conditions) on Wiley Online Library for rules of use; OA articles are governed by the applicable Creative Commons License

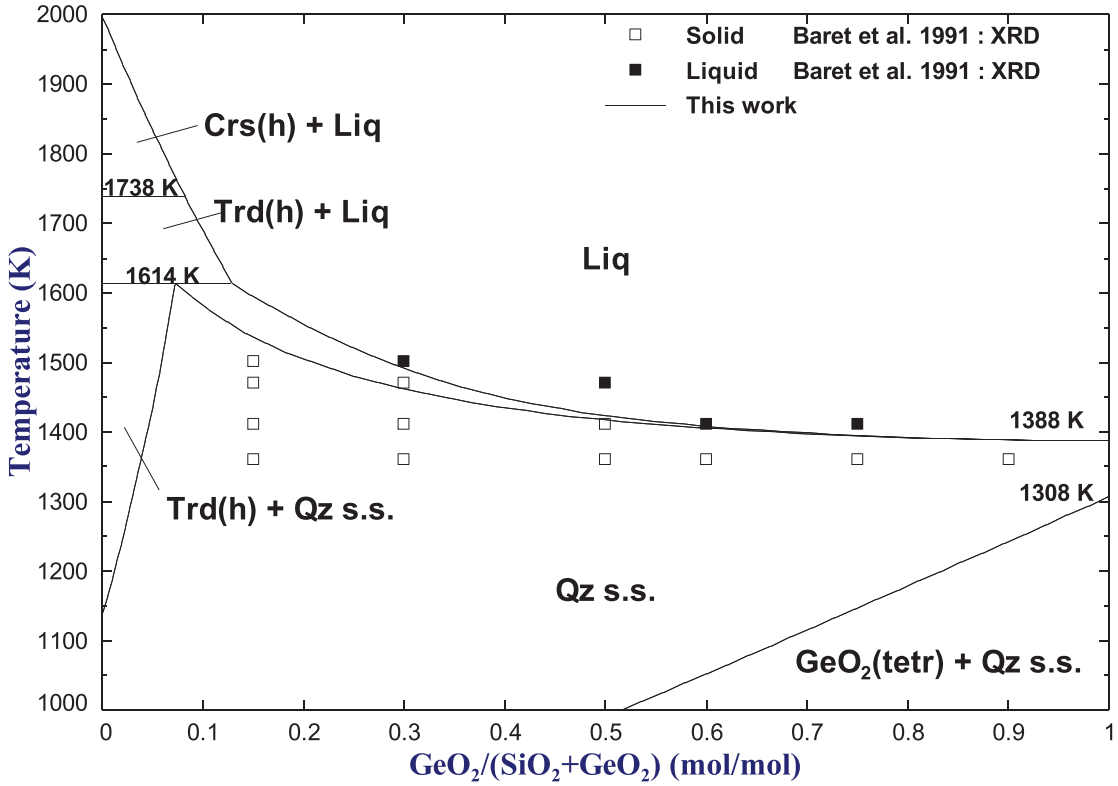

FIGURE 14 | Optimized calculated phase diagram of the GeO_2–SiO_2 binary system, along with experimental data. Liq, Qz s.s., Crs(h), Trd(h), and tetr represent liquid, quartz solid solution, cristobalite, tridymite, and tetragonal, respectively.

TABLE 9 | Calculated invariant reactions of the GeO_2–CaO and GeO_2–SiO_2 binary systems.

System	Invariant reaction	Composition (mole fraction)	Temperature (K)
GeO_2–CaO	$L \rightarrow GeO_{2(hex.)} + Ca_2Ge_7O_{16}$	0.038 CaO	1351
	$L \rightarrow Ca_2Ge_7O_{16} + CaGe_2O_5$	0.30 CaO	1551
	$L \rightarrow CaGe_2O_5 + CaGeO_3$	0.36 CaO	1544
	$L \rightarrow CaGeO_3 + Ca_3Ge_2O_7$	0.55 CaO	1657
	$L + Ca_2GeO_4 \rightarrow Ca_3Ge_2O_7$	0.60 CaO	1682
	$L \rightarrow Ca_2GeO_4 + Ca_3GeO_5$	0.70 CaO	2104
	$L + CaO \rightarrow Ca_3GeO_5$	0.75 CaO	2152
GeO_2–SiO_2	$SiO_{2(S4)} + L \rightarrow$ Quartz S.S.	0.072 GeO_2	1624

Note: L stands for the liquid phase.

supporting predictive simulations in metallurgical recycling as well as advanced ceramic-glass design and processing.

Acknowledgments

The authors gratefully acknowledge financial support from the NSERC Discovery Grant (RGPIN-2022-03847) and the Glencore Scholarship. Special thanks are extended to Drs. Mohammad Saadati (ÉTS), Victor Brial (ÉTS), and Manel Houria (ÉTS), as well as Mr. Lang Shi (McGill University), for their valuable assistance in conducting the experiments and phase characterization.

References

1. P. Meshram and Abhilash, "Strategies for Recycling of Primary and Secondary Resources for Germanium Extraction," *Mining, Metallurgy & Exploration* 39, no. 2 (2022): 689–707, https://doi.org/10.1007/s42461-022-00549-5.

2. C. Licht, L. T. Peiró, and G. Villalba, "Global Substance Flow Analysis of Gallium, Germanium, and Indium: Quantification of Extraction, Uses, and Dissipative Losses Within Their Anthropogenic Cycles," *Journal of Industrial Ecology* 19, no. 5 (2015): 890–903, https://doi.org/10.1111/jiec.12287.

3. G. A. Blengini, C. E. Latunussa, E. Umberto, et al., *Study on the EU's List of Critical Raw Materials (2020): Final Report* (Publications Office of the European Union, 2020).

15512916, 2026, 2, Downloaded from https://ceramics.onlinelibrary.wiley.com/doi/10.1111/jace.70551 by Ecole De Technologie Superieur, Wiley Online Library on [25/03/2026]. See the Terms and Conditions (https://onlinelibrary.wiley.com/terms-and-conditions) on Wiley Online Library for rules of use; OA articles are governed by the applicable Creative Commons License

4. H. Kamran Haghighi and M. Irannajad, "Roadmap for Recycling of Germanium From Various Resources: Reviews on Recent Developments and Feasibility Views," *Environmental Science and Pollution Research* 29, no. 32 (2022): 48126–48151, https://doi.org/10.1007/s11356-022-20649-5.

5. H. U. Sverdrup and H. V. Haraldsson, "Assessing the Long-Term Sustainability of Germanium Supply and Price Using the WORLD7 Integrated Assessment Model," *Biophysical Economics and Sustainability* 9, no. 4 (2024): 5, https://doi.org/10.1007/s41247-024-00121-3.

6. A. Anindya, D. R. Swinbourne, M. A. Reuter, and R. W. Matusewicz, "Distribution of Elements Between Copper and FeO_X–CaO–SiO_2 Slags During Pyrometallurgical Processing of WEEE," *Mineral Processing and Extractive Metallurgy* 122, no. 3 (2013): 165–173, https://doi.org/10.1179/1743285513Y.0000000043.

7. E. Rudnik, "Challenges and Opportunities in Hydrometallurgical Recovery of Germanium From Coal By-Products," *Molecules (Basel, Switzerland)* 30, no. 8 (2025): 1695, https://doi.org/10.3390/molecules30081695.

8. F. Liu, Z. Liu, Y. Li, B. P. Wilson, and M. Lundström, "Recovery and Separation of Gallium(III) and Germanium(IV) From Zinc Refinery Residues: Part I: Leaching and Iron(III) Removal," *Hydrometallurgy* 169 (2017): 564–570, https://doi.org/10.1016/j.hydromet.2017.03.006.

9. S. Rao, Z.-Q. Liu, D.-X. Wang, et al., "Hydrometallurgical Process for Recovery of Zn, Pb, Ga and Ge From Zn Refinery Residues," *Transactions of Nonferrous Metals Society of China* 31, no. 2 (2021): 555–564, https://doi.org/10.1016/S1003-6326(21)65517-6.

10. K. Avarmaa, S. Yliaho, and P. Taskinen, "Recoveries of Rare Elements Ga, Ge, In and Sn From Waste Electric and Electronic Equipment Through Secondary Copper Smelting," *Waste Management* 71 (2018): 400–410, https://doi.org/10.1016/j.wasman.2017.09.037.

11. M. Prasad, J. Thirupathi, S. Stalin, and C. V. More, Physical, Optical and Radiation Shielding Properties of Cao-Bi 2o 3-B 2o 3-Ge O 2 Glasses. Available at SSRN 5141534, 2025.

12. I. Bajenova, A. Khvan, M. Derevyanko, et al., "Third-Generation CALPHAD Description of Pure GeO2 at 1 Atm," *Calphad* 74 (2021): 102299, https://doi.org/10.1016/j.calphad.2021.102299.

13. A. B. Bykov, M. Y. Sharonov, V. Petricevic, et al., "Synthesis and Characterization of $Cr4^+$-Doped CaO–GeO_2–Li_2O–B_2O_3(Al_2O_3) Transparent Glass-Ceramics," *Journal of Non-Crystalline Solids* 352, no. 52–54 (2006): 5508–5514, https://doi.org/10.1016/j.jnoncrysol.2006.09.015.

14. X. Jiang, L. Su, P. Yu, et al., "Broadband Photoluminescence of Bi_2O_3–GeO_2 Binary Systems: Glass, Glass-Ceramics and Crystals," *Laser Physics* 23, no. 10 (2013): 105812, https://doi.org/10.1088/1054-660X/23/10/105812.

15. I. Koseva, V. Nikolov, M. Gancheva, et al., "Optical Properties of the Glasses From the System CaO-GeO_2-Li_2O-B_2O_3 Doped by Terbium," *Materials Today: Proceedings* 61 (2022): 1190–1197.

16. K. Baral, P. Adhikari, and W.-Y. Ching, "Ab Initio Modeling of the Electronic Structures and Physical Properties of a-Si 1− X Ge X O 2 Glass (x = 0 to 1)," *Journal of the American Ceramic Society* 99, no. 11 (2016): 3677–3684, https://doi.org/10.1111/jace.14386.

17. G. M. Rego, "Temperature Dependence of the Thermo-Optic Coefficient of GeO2-Doped Silica Glass Fiber," *Sensors* 24, no. 15 (2024): 4857, https://doi.org/10.3390/s24154857.

18. A. K. Shirvinskaya, R. G. Grebenshchikov, and N. A. Toporov, "Calcium Oxide Germanium Dioxide System," *Inorganic Materials* 2 (1966): 332–335.

19. R. G. Grebenshchikov, A. K. Shirvinskaya, V. I. Shitova, et al., "Phase Equilibria in Several Sections of the CaO-BaO-GeO_2-SiO_2 System," in 2nd All-Union Conference of the High Temperature Chemistry of Oxides, Leningrad, USSR (1967), 117–124.

20. I. Barin and G. Platzki, *Thermochemical Data of Pure Substances*, 3rd ed. (1995), https://doi.org/10.1002/9783527619825.

21. M. Yonemura and Y. Kotera, "Kinetic Study on the Phase Transformation of GeO_2," in *Reactivity of Solids*, ed. J. Wood, O. Lindqvist, C. Helgesson, and N. G. Vannerberg (1977), 227–232, https://doi.org/10.1007/978-1-4684-2340-2.

22. G. R. Newns and R. Hanks, "Thermal Behaviour of Germanium Dioxide," *Journal of the Chemical Society A: Inorganic, Physical, Theoretical* (1966): 954–957, https://doi.org/10.1039/J19660000954.

23. P. Richet, "GeO_2 vs SiO_2: Glass Transitions and Thermodynamic Properties of Polymorphs," *Physics and Chemistry of Minerals* 17, no. 1 (1990): 79–88, https://doi.org/10.1007/BF00209228.

24. A. T. Dinsdale, A. Akhmetova, A. V. Khvan, and N. Aristova, "A Critical Assessment of Thermodynamic and Phase Diagram Data for the Ge-O System," *Journal of Phase Equilibria and Diffusion* 36, no. 3 (2015): 254–261, https://doi.org/10.1007/s11669-015-0379-1.

25. L. V. Gurvich, I. V. Veyts, and C. B. Alcock, *Thermodynamic Properties of Individual Substances: Elements and Compounds*, Vol. 2 (1990).

26. J. F. Counsell and J. F. Martin, "The Entropy of Tetragonal Germanium Dioxide," *Journal of the Chemical Society A: Inorganic, Physical, Theoretical* (1967): 560–561, https://doi.org/10.1039/J19670000560.

27. R. J. L. Andon and K. C. Mills, "The Heat Capacity of Tetragonal Germanium Dioxide," *Journal of Chemical Thermodynamics* 3, no. 4 (1971): 583–587, https://doi.org/10.1016/S0021-9614(71)80042-3.

28. E. G. King, "Low Temperature Heat Capacities and Entropies at 298.15°K. of Some Oxides of Gallium, Germanium, Molybdenum and Niobium," *Journal of the American Chemical Society* 80, no. 8 (1958): 1799–1800, https://doi.org/10.1021/ja01541a005.

29. K. K. Kelley and A. U. Christensen, *High-Temperature Heat Content and Entropies of Crystalline and Glassy Germanium Dioxide* (U.S. Dept. of the Interior, Bureau of Mines, 1960).

30. V. V. Tarasov and Z. Soboleva, "Heat Capacity of Vitreous GeO_2 and Glasses in the K_2O–GeO_2 System," *Russian Journal of Physical Chemistry* 44, no. 6 (1970): 1590–1592.

31. V. I. Davydov, "Study of Equilibrium Vapor Pressures of Germanium Dioxide," *Journal of Inorganic Chemistry* 2 (1957): 1460–1466.

32. T. Sasamoto, M. Kobayashi, and T. Sata, "Mass Spectrometric Measurement of GeO_2 (g) Partial Pressure on GeO_2 and a Consideration on the Molecular Structure of Ge_3O_3 (g)," *Journal of the Mass Spectrometry Society of Japan* 29, no. 3 (1981): 249–255, https://doi.org/10.5702/massspec.29.249.

33. E. Shimazaki, N. Matsumoto, and K. Niwa, "The Vapor Pressure of Germanium Dioxide," *Bulletin of the Chemical Society of Japan* 30, no. 9 (1957): 969–971, https://doi.org/10.1246/bcsj.30.969.

34. A. S. Smirnov, K. G. Smorchkov, N. A. Gribchenkova, and A. S. Alikhanyan, "Vaporization Thermodynamics of GeO_2 by High-Temperature Mass Spectrometry," *Doklady Physical Chemistry* 501, no. 2 (2021): 119–125, https://doi.org/10.1134/S0012501621120010.

35. E. H. Copland and N. S. Jacobson, "Measuring Thermodynamic Properties of Metals and Alloys With Knudsen Effusion Mass Spectrometry," NASA Technical Reports Server (2010).

36. T. Bgasheva, T. Falyakhov, S. Petukhov, M. Sheindlin, A. Vasin, and P. Vervikishko, "Laser-Pulse Melting of Calcium Oxide and Some Peculiarities of Its High-Temperature Behavior," *Journal of the American Ceramic Society* 104, no. 7 (2021): 3461–3477, https://doi.org/10.1111/jace.17676.

37. D. Manara, R. Böhler, L. Capriotti, et al., "On the Melting Behaviour of Calcium Monoxide Under Different Atmospheres: A Laser Heating Study," *Journal of the European Ceramic Society* 34, no. 6 (2014): 1623–1636, https://doi.org/10.1016/j.jeurceramsoc.2013.12.018.

38. M. Foex, "Measurement of the Solidification Points of Several Refractory Oxides by Means of a Solar Furnace," *Solar Energy* 9, no. 1 (1965): 61–67, https://doi.org/10.1016/0038-092X(65)90162-3.

39. T. Yamada, M. Yoshimura, and S. Sōmiya, "Reinvestigation of the Solidification Point of CaO by Digital Pyrometry," *Journal of the American*

15512916, 2026, 2, Downloaded from https://ceramics.onlinelibrary.wiley.com/doi/10.1111/jace.70551 by Ecole De Technologie Superieur, Wiley Online Library on [25/03/2026]. See the Terms and Conditions (https://onlinelibrary.wiley.com/terms-and-conditions) on Wiley Online Library for rules of use; OA articles are governed by the applicable Creative Commons License

Ceramic Society 69, no. 10 (1986): C-243–C-245, https://doi.org/10.1111/j.1151-2916.1986.tb07350.x.

40. R. C. Doman, J. B. Barr, R. N. Mcnally, and A. M. Alper, "Phase Equilibria in the System CaO—MgO," *Journal of the American Ceramic Society* 46, no. 7 (1963): 313–316, https://doi.org/10.1111/j.1151-2916.1963.tb11737.x.

41. C. W. Kanolt, *Melting Points of Some Refractory Oxides* (U.S. Department of Commerce, Bureau of Standards, 1914).

42. T. Noguchi, M. Mizuno, and W. M. Conn, "Fundamental Research in Refractory System With a Solar Furnace ZrO-CaO System," in Solar Energy Conference, Phoenix, Arizona (1967).

43. Z. Panek, "Melting Temperatures of CaO and MgO," *Silikaty* 23 (1979): 97–102.

44. E. E. Schumacher, "Melting Points of Barium, Strontium and Calcium Oxides 1," *Journal of the American Chemical Society* 48, no. 2 (1926): 396–405, https://doi.org/10.1021/ja01413a013.

45. C. M. S. Alvares, G. Deffrennes, A. Pisch, and N. Jakse, "Thermodynamics and Structural Properties of CaO: A Molecular Dynamics Simulation Study," *Journal of Chemical Physics* 152, no. 8 (2020): 084503, https://doi.org/10.1063/1.5141841.

46. F. Menescardi, D. Ceresoli, and D. Belmonte, "Melting Behavior of CaO at High Temperature and Pressure: A Molecular Dynamics Study," *Journal of Physical Chemistry C* 128, no. 43 (2024): 18498–18508, https://doi.org/10.1021/acs.jpcc.4c04752.

47. W.-G. Seo and F. Tsukihashi, "Molecular Dynamics Simulation of the Thermodynamic and Structural Properties for the CaO-SiO2 System," *ISIJ International* 44, no. 11 (2004): 1817–1825, https://doi.org/10.2355/isijinternational.44.1817.

48. X.-W. Wang, X.-W. Sun, T. Song, J.-H. Tian, and Z.-J. Liu, "Prediction of the Melting Curve and Phase Diagram for CaO Using Newly Developed Interatomic Potentials," *Vacuum* 209 (2023): 111717, https://doi.org/10.1016/j.vacuum.2022.111717.

49. G. Eriksson, P. Wu, M. Blander, and A. D. Pelton, "Critical Evaluation and Optimization of the Thermodynamic Properties and Phase Diagrams of the MnO–SiO2 and CaO–SiO2 Systems," *Canadian Metallurgical Quarterly* 33, no. 1 (1994): 13–21, https://doi.org/10.1179/cmq.1994.33.1.13.

50. M. W. Chase, C. A. Davies, J. R. Jr. Downey, et al., "NIST-JANAF Thermochemical Tables," in *Standard Reference Data Program* (National Institute of Standards and Technology, 1985).

51. S. M. Royak and I. A. Prokhvatilova, *Calcium Germanates and Their Properties* (1961).

52. T. Hahn and W. Eysel, "Struktur und Polymorphie von Tricalciungermanat," *Die Naturwissenschaften* 50, no. 13 (1963): 471–471, https://doi.org/10.1007/BF00632916.

53. W. L. W. Ludekens, "The Preparation of Orthogermanates by Sintering Reactions: Some New Germanates of the Type A2GeO4," *Journal of Inorganic and Nuclear Chemistry* 3, no. 5 (1956): 281–284, https://doi.org/10.1016/0022-1902(56)80036-5.

54. V. F. Zhuravlev, "Some Regularities in the Field of Chemistry of Binding Substances," *Journal of Applied Chemistry* 13, no. 8 (1940): 1141.

55. V. F. Zhuravlev, "Calcium Orthogermanate and Its Binding Properties," *Reports of the Academy of Sciences of the USSR* 59, no. 6 (1947): 1145.

56. G. Eulenberger, A. Wittmann, and H. Nowotny, "Germanates With Divalent Metal Ions," *Chemical Monthly* 93, no. 5 (1962): 1046–1054, https://doi.org/10.1007/BF00905903.

57. N. A. Toropov and A. K. Shirvinskaya, "Solid Solutions in the Ca_2SiO_4–Ca_2GeO_4 System," *Reports of the Academy of Sciences of the USSR* 153, no. 5 (1963): 1081–1084.

58. M. O. Marychev, I. Koseva, G. Gencheva, R. Stoyanova, R. Kukeva, and V. Nikolov, "Cr Doped Ca_2GeO_4, $Ca_5Ge_3O_{11}$ and Li_2CaGeO_4 Single Crystals Grown by the Flux Method," *Journal of Crystal Growth* 461 (2017): 46–52, https://doi.org/10.1016/j.jcrysgro.2017.01.003.

59. H. Koelmans and C. M. C. Verhagen, "The Fluorescence of Binary and Ternary Germanates of Group II Elements," *Journal of the Electrochemical Society* 106, no. 8 (1959): 677, https://doi.org/10.1149/1.2427470.

60. M. Catauro, S. Gargano, and G. Laudisio, "The Non-Isothermal Devitrification of Glasses in the CaO·4GeO2–BaO·4GeO2 Composition Range," *Thermochimica Acta* 356 (2000): 127–131, https://doi.org/10.1016/S0040-6031(00)00472-X.

61. G. J. Redhammer, G. Roth, and G. Amthauer, "Dicalcium Heptagermanate $Ca_2Ge_7O_{16}$ Revised," *Acta Crystallographica Section C Crystal Structure Communications* 63, no. 7 (2007): i47–i50, https://doi.org/10.1107/S010827010702269X.

62. C. R. Robbins and E. M. Levin, "The System Magnesium Oxide-Germanium Dioxide," *American Journal of Science* 257, no. 1 (1959): 63–70, https://doi.org/10.2475/ajs.257.1.63.

63. A. N. Shushunov, O. N. Gorshkov, N. N. Smirnova, et al., "Thermophysical Properties of Ca_2GeO_4 over the Temperature Range Between (6 and 350)K," *Journal of Chemical Thermodynamics* 78 (2014): 58–68, https://doi.org/10.1016/j.jct.2014.06.019.

64. J. P. Coughlin and C. J. O'Brien, "High Temperature Heat Contents of Calcium Orthosilicate," *Journal of Physical Chemistry* 61, no. 6 (1957): 767–769, https://doi.org/10.1021/j150552a016.

65. G. Baret, R. Madar, and C. Bernard, "Silica-Based Oxide Systems: I. Experimental and Calculated Phase Equilibria in Silicon, Boron, Phosphorus, Germanium, and Arsenic Oxide Mixtures," *Journal of the Electrochemical Society* 138, no. 9 (1991): 2830–2835, https://doi.org/10.1149/1.2086066.

66. V. Swamy, S. A. Decterov, and A. D. Pelton, "Thermodynamic Assessment of the Ge-Si-O-Cl-H System," *Glass Science and Technology* 76 (2003): 62–70.

67. M. Huffman, A. Navrotsky, and F. S. Pintchovski, "Thermochemistry and Structure of Low Pressure Chemically Vapor Deposited and Bulk SiO2 - P2O5 and SiO2 - GeO2 Glasses," *Journal of the Electrochemical Society* 133, no. 2 (1986): 431–439, https://doi.org/10.1149/1.2108593.

68. P. D. Maniar, A. Navrotsky, and C. W. Draper, "Thermochemistry of the Amorphous System SiO 2-GeO 2: Comparison of Flame Hydrolysis Materials to High Temperature Fused Glasses," *MRS Proceedings* 172 (1989): 15, https://doi.org/10.1557/PROC-172-15.

69. M. Micoulaut, L. Cormier, and G. S. Henderson, "The Structure of Amorphous, Crystalline and Liquid GeO_2," *Journal of Physics: Condensed Matter* 18, no. 45 (2006): R753–R784.

70. A. D. Pelton, "Thermodynamic Origin of Phase Diagrams," in *Phase Diagrams and Thermodynamic Modeling of Solutions* (Elsevier, 2019).

71. A. D. Pelton, S. A. Degterov, G. Eriksson, C. Robelin, and Y. Dessureault, "The Modified Quasichemical Model I—Binary Solutions," *Metallurgical and Materials Transactions B* 31, no. 4 (2000): 651–659, https://doi.org/10.1007/s11663-000-0103-2.

72. I.-H. Jung, S. A. Decterov, and A. D. Pelton, "Critical Thermodynamic Evaluation and Optimization of the CaO–MgO–SiO_2 System," *Journal of the European Ceramic Society* 25, no. 4 (2005): 313–333, https://doi.org/10.1016/j.jeurceramsoc.2004.02.012.

73. P. Armand, D. Granier, and M. Tillard, "A Complete Solid Solution Between GeO2 and SiO2 With the α-Quartz Structure: Additional X-Ray Diffraction Data From Ge1Si O2 Flux-Grown Crystals," *Journal of Solid State Chemistry* 317 (2023): 123658, https://doi.org/10.1016/j.jssc.2022.123658.

74. M. Hillert, "The Compound Energy Formalism," *Journal of Alloys and Compounds* 320, no. 2 (2001): 161–176, https://doi.org/10.1016/S0925-8388(00)01481-X.

75. R. S. Mikhail, S. Brunauer, and L. E. Copeland, "Kinetics of the Thermal Decomposition of Calcium Hydroxide," *Journal of Colloid and*

15512916, 2026, 2, Downloaded from https://ceramics.onlinelibrary.wiley.com/doi/10.1111/jace.70551 by Ecole De Technologie Superieur, Wiley Online Library on [25/03/2026]. See the Terms and Conditions (https://onlinelibrary.wiley.com/terms-and-conditions) on Wiley Online Library for rules of use; OA articles are governed by the applicable Creative Commons License

Interface Science 21, no. 4 (1966): 394–404, https://doi.org/10.1016/0095-8522(66)90005-5.

76. L. P. Cook and E. R. Plante, "Phase Diagram of the System Li_2O-Al_2O_3," *Ceramic Transactions* 27 (1992): 193–222.

77. B. Konar, D.-G. Kim, and I.-H. Jung, "Coupled Phase Diagram Experiments and Thermodynamic Optimization of the Binary Li_2O-MgO and Li_2O-CaO Systems and Ternary Li_2O-MgO-CaO System," *Ceramics International* 43, no. 16 (2017): 13055–13062, https://doi.org/10.1016/j.ceramint.2017.06.143.

78. W. J. Boettinger, U. R. Kattner, K.-W. Moon, et al., "DTA and Heat-Flux DSC Measurements of Alloy Melting and Freezing," in *Methods for Phase Diagram Determination* (2007).

79. J. F. Sarver and F. A. Hummel, "Alpha to Beta Transition in Germania Quartz and a Pressure-Temperature Diagram for GeO 2," *Journal of the American Ceramic Society* 43, no. 6 (1960): 336–336, https://doi.org/10.1111/j.1151-2916.1960.tb13665.x.

80. R. A. Brooker and B. A. Kjarsgaard, "Silicate–Carbonate Liquid Immiscibility and Phase Relations in the System SiO2–Na2O–Al2O3–CaO–CO2 at 0·1–2·5 GPa With Applications to Carbonatite Genesis," *Journal of Petrology* 52, no. 7–8 (2011): 1281–1305, https://doi.org/10.1093/petrology/egq081.

81. R. G. Grebenshchikov and N. A. Toropov, "Solid Solutions of Ba_2SiO_4–Ba_2GeO_4," *Reports of the Academy of Sciences of the USSR* 1, no. 1 (1965): 121–125.

82. S. K. Gupta, K. Sudarshan, and R. M. Kadam, "Optical Nanomaterials With Focus on Rare Earth Doped Oxide: A Review," *Materials Today Communications* 27 (2021): 102277, https://doi.org/10.1016/j.mtcomm.2021.102277.

83. P. Gross, C. Hayman, and J. T. Bingham, "Heats of Formation of Germanium Tetrafluoride and of the Germanium Dioxides," *Transactions of the Faraday Society* 62 (1966): 2388, https://doi.org/10.1039/tf9666202388.

84. J. A. Arias Hernandez and E. Moosavi-Khoonsari, "Modified Polyhedron Model for Predicting Standard Enthalpy of Formation and Entropy of Mixed Oxides," *Calphad* 90 (2025): 102848, https://doi.org/10.1016/j.calphad.2025.102848.

15512916, 2026, 2, Downloaded from https://ceramics.onlinelibrary.wiley.com/doi/10.1111/jace.70551 by Ecole De Technologie Superieur, Wiley Online Library on [25/03/2026]. See the Terms and Conditions (https://onlinelibrary.wiley.com/terms-and-conditions) on Wiley Online Library for rules of use; OA articles are governed by the applicable Creative Commons License